Simulation and Detection of Cherenkov Light in Water Neutrino Detectors

by

Dmytro Minchenko

A thesis submitted in partial fulfillment of the requirements for the degree of

Master of Science

Department of Physics
University of Alberta

Abstract

Cherenkov light plays a crucial role in particle physics and is used in a wide variety of neutrino experiments to observe the secondary charged particles created after neutrino interaction. In this thesis, we consider two ways to improve both the simulation of Cherenkov light and the design of devices for its detection.

First, we examine the approximation of the Cherenkov light coherent emission along the whole track of a charged particle used by the MC simulation tools, Geant4 in particular. We use a more physically accurate scattering model to precisely simulate particle propagation in a medium and calculate the Cherenkov light profile as the interference of the electromagnetic waves. We conclude that the Cherenkov radiation is coherent when electrons with energies down to 0.3 MeV travel in water, but a choice of a scattering model used for the simulation significantly changes the angular distribution of the emitted Cherenkov light. As a result, we develop a new Cherenkov radiation model for MC simulations and tune it in the 2.2 - 6.1 MeV energy range using SNO+ calibration data obtained from AmBe and ^{16}N radioactive sources. With this model we resolve a previously observed tension in the isotropy of the Cherenkov light in SNO+, significantly improving how the simulation describes the data.

With future Cherenkov detectors in mind, we also develop a simulation to assist in the design of silicon photomultipliers (SiPMs). The specific goal is to reduce the level of optical crosstalk (OCT) in the devices. The code is verified by comparing the obtained crosstalk levels to data from two SiPMs Hamamatsu VUV4 and FBK HD3 SiPMs. The code will be used to find the optimal geometry parameters to minimize OCT levels of possible future SiPM designs that will be capable of better light detection.

Preface

The work described in this thesis was done in conjunction with 2 different experimental collaborations: SNO+ and JADDE. Usage of work other than the author's is properly cited in the text.

The theoretical results and discussions in Chapter 2 are a review of the literature at the time of writing the thesis. All the simulations and calculations were performed by the author. The results from this chapter were presented at CAP 2021.

The SNO+ calibration group deployed the ^{16}N and AmBe sources mentioned in Chapter 3. The calibration data was gathered by the SNO+ detector, which requires the effort of the whole collaboration. The author used these data to produce custom simulations and calibrate the model proposed in Chapter 3. Reconstruction algorithms and selection criteria used for ^{16}N and AmBe events identification were developed by the SNO+ collaboration. An abstract describing the results of this chapter was accepted to 11th International Workshop on Ring Imaging Cherenkov Detectors.

In Chapter 4, the simulation work was originally started in TRIUMF in the group of Fabrice Retière. The author expanded the possibilities of the simulation code and develops a new analysis technique with the help of JADDE collaboration members. The results of this chapter work were presented at CAP 2022.

Acknowledgements

First, I want to thank my supervisor Juan Pablo Yáñez for the last more than 2 years of teaching and managing me and explaining how the science works. I appreciate him giving me a lot of scientific freedom but always being there for avid, and somehow intense discussions when I was stuck on a problem. Also, thanks to Aksel Hallin and Carsten Krauss for the many comments and feedback they gave me during the group meetings. I would like to thank Jie Hu and Yang Zhang for helping me figure out how the SNO+ analysis works. Big thanks to the other members of the University of Alberta SNO+ group: Ankit Gaur, David Auty, John Wilson, Karl Yazigi, and Shaokai Yang – who were patient with me and my long presentations. It was also a pleasure to work with and learn about the lab hardware from Logan Sibley.

I would like to thank Fabrice Retière for the advice and insight regarding the development of new SiPMs, and for the conference rehearsal at the pool. I want to mention Aleksey Sher, who introduced me to the simulation software; Paolo Agnes, Frédéric Vachon, and Giacomo Gallina for the private discussions and a lot of feedback during the meetings. I also would like to express my gratitude to all of the other members of the SNO+ and JADDE collaborations, whose input contributed to my work.

I'd like to say thank you, again, to Juan Pablo and Caitlin, who were there for me from my very first day in Canada, helping me to figure out a whole new life and instilling love to spicy food. Thanks to my very first friend in Edmonton and my office mate Nakul. We both had hardships of COVID, moving, classes, research and having someone who was going through the same thing was so important to me. I am grateful to Tatiana for many fun trips and helping me make it through the COVID times sane. I want to mention an amazing group of incredible people who made my life in Edmonton so much better: Abraham, Alex, Karl, Santiago, Lupita – thank you for everything, and for H2O nights in particular. I will be missing long training sessions with Pol and Elisabeth, who endured my whining and became my friends. I want to thank Tian, who's the best labmate and the best white elephant player. Thank you, Kalley, for understanding and being around unconditionally, and, of course, for the proofreading.

I want to say a huge thanks to my family, who by all means made it possible for me now being able to write this thesis. Especially to my mother Olena, who supported my studies even in the hardest time of her life. Also, thanks for the huge, even though remote, support to my old good friends Igor, Nadia, Alex, and Vita.

Last but not least I want to thank Volodymyr Aushev for being the person who believed in me and guided me into particle physics.

Contents

List of Tables

List of Figures

Chapter 1

Introduction

The history of Cherenkov light starts at the beginning of the 1930s when Pavel Cherenkov began studying luminescence of uranyl salt solutions that were irradiated by γ-rays of a radium source. During the experiments, Cherenkov noticed a faint blue light-induced by electrons created by γ - radiation in one of the solutions. Further observations confirmed that this light does not depend on the concentration, temperature, and viscosity of the liquid. This light was clearly distinguishable from the luminescence light and turned out to be partially polarized. The polarization plane was mostly parallel to the direction of γ-rays propagation [1, 2].

The results of the Cherenkov investigation were explained theoretically by Tamm and Frank in 1937 [3]. Based on classical electrodynamics they established a spatial asymmetry of the radiation and the proportionality between the electron path in a medium and its radiated light intensity. Both of these predictions were confirmed in later experiments [4]. The results were also confirmed by Railing [5] and Wyckoff and Henderson [6].

In the 1930s only an eye could detect dim Cherenkov light, but photomultiplier tube (PMT) development in the 40s made it possible to detect the very weak flux of light on the level of single photons. This led to the emergence of detectors based on the Cherenkov effect. Threshold Cherenkov detectors and later Ring-imaging Cherenkov detectors appeared [7] and became a mechanism to distinguish different types of charged particles in high energy physics experiments.

Apart from that, the Cherenkov effect is used in a variety of astroparticle physics experiments like IceCube, SNO+, and Super Kamiokande. These detectors intend to detect neutrino – a neutral, spin-1/2 fermion that interacts only via weak interactions and gravity. The experiments use water or ice as the active region where charged particles from neutrino interactions with the medium produce Cherenkov light. Then the light is detected by arrays of photomultipliers, and through the analysis of the acquired light, the properties of the charged particles are obtained. To make more precise measurements possible with a new generation of astroparticle Cherenkov detectors we need to reassess the accuracy of our modeling of Cherenkov light, as well as improve our photodetectors to have better time and charge resolution than PMTs. A technology that qualifies for that is a silicon photomultiplier (SiPM) [8]. It is widely used in medicine, and biology, and is being considered for use in some particle physics experiments [9]. It has improved charge and time resolution compared to the PMTs, however, the comparatively high intrinsic noise poses challenges for its use in neutrino experiments.

1.1 Motivation

Neutrinos are elementary particles in the most successful theory that describes the properties and interactions of all elementary particles we have so far observed – the Standard Model (SM). The existence of the neutrino was proposed in 1930 by Pauli with the first experimental detection in 1956 from a nuclear reactor [10]. As of now, evidence from particle decays [11, 12] suggest there are only three light, active neutrino types (flavors). Neutrinos are produced via the weak force in particle decays. Nature produces them abundantly in the Sun, cosmic ray interactions in the atmosphere, Earth's core, and astrophysical objects, while scientists use nuclear reactors and accelerators to create neutrinos [13]. Studying these sources led to the confirmation that neutrinos are changing their type on their way through the space and matter

[14, 15]. This discovery tells us that neutrinos have a non-zero mass, which albeit small contradicts the original SM postulate and brings up new questions on their mass generation mechanism as well as the structure behind the mixing of their mass and flavor states. These questions are among the most pressing ones in particle physics today, and testing theories that seek to address them [16, 17] is a very active field of experimental research.

Particle physics experiments observe and identify particles by the way they interact with matter. Neutrinos are neutral and have a very small mass, thus for their detection we need to rely on the particles they produce when they interact. Since they only interact weakly, their interaction probability is small, so detectors have to be massive.

One way to overcome the large masses required is to instrument large volumes of water with photomultiplier tubes to detect the Cherenkov light emitted as a result of neutrino interactions. Cherenkov photons are emitted in a direction that is correlated to the charged particle responsible for it, so using it one can infer the particle's direction. Moreover, the number of Cherenkov photons is proportional to the path length, which can be connected to the particle's energy. Experiments like Super Kamiokande [18], IceCube [19], and ANTARES [20] utilize this effect. Some efforts seek to combine it with other detection techniques, like the use of scintillation light, to take advantage of event direction reconstruction and high sensitivity in low energy region. THEIA [21] experiment is going to use both Cherenkov light and scintillation techniques at the same time as the detection mechanism.

An important part of the analysis techniques in these experiments is Monte-Carlo simulations. The most widely used package for this task in particle physics is Geant4 [22]. The further development of this package and its improvement continues constantly thanks to the contribution of people from different particle physics experiments. The Sudbury Neutrino Observatory (SNO+) also uses this framework as the basis for its simulation software and has observed a discrepancy between Monte-Carlo and data Cherenkov light distributions. We study this discrepancy to improve the experiment's systematic errors and contribute to Geant4, making the simulation more accurate, which is necessary for future, more sensitive Cherenkov light detectors. To contribute more towards a new generation of detectors we also look into SiPMs development and collaborate with other Canadian institutions to improve the light detection capabilities of such a device.

1.2 Thesis Objectives and Outline

The goal of this work is to improve Cherenkov light simulation and detection, and, as the result, decrease systematic errors in the SNO+ experiment as well as enable increased precision in next-generation water-neutrino detectors. The thesis is divided in 3 parts:

1. We explore the nature of Cherenkov light as an interference effect and investigate the influence of scattering of a charged particle on the total angular distribution of the radiation. We also study whether the Geant4 assumptions for production of Cherenkov light hold for low energy electrons propagating in water.

2. We study the Geant4 simulation of the SNO+ detector and use its calibration data to understand the MC output response to changes in the Cherenkov light emission. We develop a new Cherenkov light radiation model for Geant4, resolving the tension between the data and Monte-Carlo simulation.

3. We describe the principles of SiPMs operation and challenges of its development, introducing optical crosstalk. We design a simulation tool for its prediction and verify the simulation. Thus, we contribute to SiPM simulations design that is required for the development of new models tailored for specific particle physics applications.

Chapter 2

Influence of scattering and interference effects on Cherenkov light emission

2.1 Cherenkov light and its simulation

Cherenkov radiation is a widely used tool in particle physics, astrophysics, nuclear physics, and medicine. Some of the astrophysics experiments are based on detection of the Cherenkov light rings to access the direction of the light emitter movement. This require high precision simulations where the correct Cherenkov radiation profile is necessary.

2.1.1 Cherenkov light classic theory

According to [3, 23] in a dielectric material with the refractive index n a charged particle that moves in a straight line with the constant speed $\beta = \frac{v}{c}$ will emit photons in Cherenkov angle θ_C between the direction of particle propagation and photon emission. This angle is defined as

$$\cos\theta_C = \frac{1}{\beta n}. \tag{2.1}$$

Note, that $n = n(\epsilon_p)$ is a function of the photon's energy. The average number of emitted photons is given by

$$dN = \frac{\alpha z^2}{\hbar c}\sin^2\theta d\epsilon dx = \frac{\alpha z^2}{\hbar c}(1 - \frac{1}{n^2\beta^2})d\epsilon dx \approx 370 z^2(1 - \frac{1}{n^2\beta^2})d\epsilon dx, \tag{2.2}$$

where α is fine-structure constant, z is an atomic charge of the medium, $\hbar$ is Planck's constant, and c is the speed of light. After integrating eq. (2.2) over ϵ we get the number of photons emitted per unit of length

$$\frac{dN}{dx} \approx 370z^2 \int_{\epsilon_{min}}^{\epsilon_{max}} d\epsilon \left(1 - \frac{1}{n^2\beta^2}\right) = 370z^2 \left[\epsilon_{max} - \epsilon_{min} - \frac{1}{\beta^2} \int_{\epsilon_{min}}^{\epsilon_{max}} \frac{d\epsilon}{n^2(\epsilon)}\right], \quad (2.3)$$

where ϵ_{min} is defined by $n(\epsilon_{min}) = \frac{1}{\beta}$ and ϵ_{max} is the maximum energy of emitted photons that are still transparent to the medium and will not be immediately reabsorbed.

2.1.2 Simulation of Cherenkov light in Geant4

Geant4 [22] is a very versatile and reliable package that is used for the simulations of many particle physics experiments. It is capable of simulating interactions of elementary particles propagating though the medium on the energy scale from eV to TeV. In particular, it is used for simulations of the water filled neutrino detector SNO+ described in Section 3.1.

Following [24], in order to simulate Cherenkov radiation with Geant4, we calculate the Cherenkov angle and the number of photons per track length using eq. (2.1) and eq. (2.3). The simulation of particle propagation in Geant4 is done in steps. The package takes the conditions of the particle at an initial point, then calculates its displacement, energy loses, and possible changes of the state; creating a post-step point that is the initial point for the next step. To get the number of photons per step, Geant4 uses eq. (2.3) and finds the mean value $\langle N \rangle = StepLength \cdot \frac{dN}{dx}$, where $StepLength$ is the length of the Geant4 step. Using this mean value, Geant4 samples the number of photons per step from a Poisson distribution.

The Cherenkov photons are emitted into a cone with the half angle of θ_C, calculated with eq. (2.1), with respect to the charged particle trajectory. Therefore, we also need to explore the way particles are propagated in the simulation and study its influence on the Cherenkov light emission.

2.2 Scattering models

Monte-Carlo simulations of particle propagation through a medium can be divided into two groups, detailed and condensed [25]. The latter describes the averaged particle displacement and energy loses after several physical interactions, while the detailed algorithms simulate each interaction and are more accurate. Within Geant4 these models are called scattering models. The model defines a step size and lateral displacement of a particle along the step. Since the detailed simulation has many more simulation steps than the condensed algorithm, it is extremely computationally expensive. Therefore, for propagation of high energy particles with high number of interactions, Geant4 usually uses condensed simulation algorithms, in particular, Multiple Scattering (MS) models like Urban [25], Penelope [26], Wentzel [27]. The step size of the condensed model can be shortened artificially to increase the precision of the simulation. The results of such a tuning can be seen on fig. 2.1 for energy deposition profile of low energy electrons [27]. Decreasing the step size makes the radioactive dose profile agree better with data. However, the most precise simulation is obtained by using the Single Scattering (SS) model. It is a Geant4 implementation of a detailed simulation model based on a Mott cross-section calculation that describes every interaction of an electron with the matter while propagating within a medium. From [28], the differential Mott cross section for the SS model is given by

$$\frac{d\sigma^{Mott}(\theta)}{d\Omega} = \frac{d\sigma^{Rut}}{d\Omega}\mathfrak{F}^2(\theta)\mathcal{R}^{Mott}|F(q)|^2. \tag{2.4}$$

For the basis, it takes a Rutherford cross section:

$$\frac{d\sigma^{Rut}}{d\Omega} = \left(\frac{Ze^2}{2mc^2\beta^2\gamma}\right)^2 \frac{1}{sin^4(\theta/2)}, \tag{2.5}$$

where m is electron rest mass, Z is the atomic number of the target nuclei, γ is Lorentz factor and θ is the scattering angle of the electron.

$\mathcal{R}^{Mott}$ is a Mott correction to the Rutherford model to obtain an approximated differential cross section that takes into effects related to the spins of electrons. In [28], authors use Lijian's, Quing's and Zhengming's [29] interpolated expression, which is valid for electron energy from several keV to hundreds MeV

$$\mathcal{R}^{Mott} = \sum_{j=0}^{4} a_j(Z, \beta)(1 - \cos\theta)^{j/2}, \tag{2.6}$$

where

$$a_j(Z, \beta) = \sum_{k=1}^{6} b_{k,j}(Z)(\beta - \overline{\beta})^{k-1}, \tag{2.7}$$

with $\overline{\beta}$ as the mean β of electrons within the model validity range and with $b_{k,j}(Z)$ coefficients listed in [29]. Because of the complicated charge distribution of atoms, they also take into account for effective change of the potential with the screening factor:

$$\mathfrak{F}^2(\theta) = \frac{\sin^2\theta/2}{A_{s,M} + \sin^2\theta/2}, \tag{2.8}$$

which depends on a screening parameter $A_{s,M}$ and scattering angle θ. Detailed discussion on $A_{s,M}$ can be found in Section 4 of [30]. Finally, they consider the finite nuclear size by introducing a nuclear form factor $F(q)$, which depends on the momentum transfer q from electron to the target. Many types of possible form factors are described in Section 2.3 of [28] and references therein. However, they conclude that any of the models are expected to be appropriate for electron single scattering mechanism.

The Urban MS model, with such a step limit that only 4 Cherenkov photons on average can be emitted along the step, is used in SNO+ simulations by default and we will refer to it as "the default SNO+ MS model" further in the text. We explore how switching from the default MS model to the SS model for electrons propagation influences the Cherenkov light angular distribution.

2.3 Comparison of scattering models in Geant4

From [24], we know that in order to create a Geant4 application for particle propagation, there are necessary parts that one has to define:

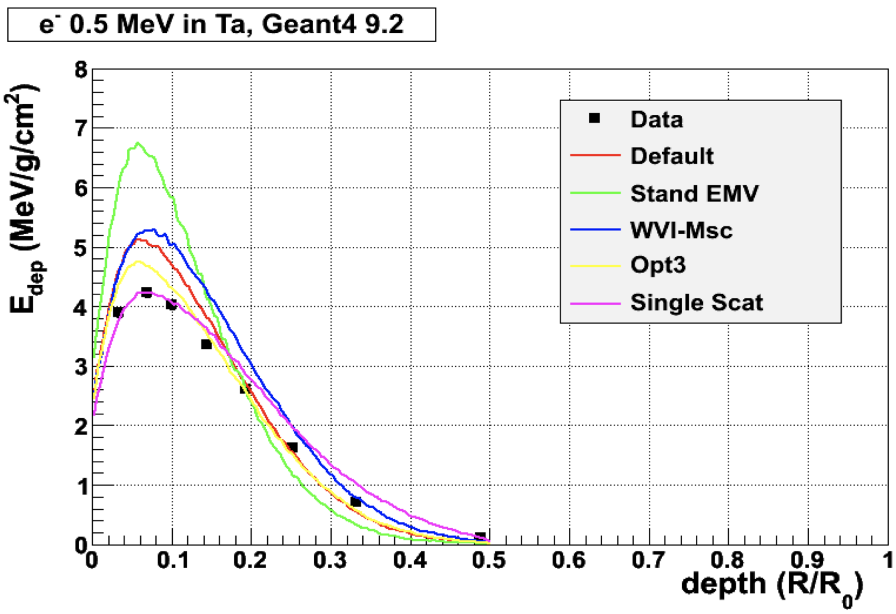

Figure 2.1: Radioactive dose profile of 0.5 MeV electron beam in Tantalum as a function of scaled thickness R/R_0, where R is the actual thickness and R_0 is the total width of the media [27]. Simulation results where single scattering model was used for the electrons propagation (magenta line) fit data the best comparing to the multiple scattering models (other colors). In multiple scattering models the comparison is done between the multiple scattering (MS) model used in Geant4 by default (Default); a MS model with minimal step limitations (Stand EMV), approximately 20 times bigger steps than in Default; Opt3 that has the strictest possible step limitations for the MS model (See [31, 32] for further details); Wentzel-VI MSC that is a mix of the default MS and SS models where the degree of mixing between two models is defined by an additional parameter described in [27], but the default value is used to obtain the blue line.

1. Geometry - volumes, materials the volumes are made of, physical properties of the material, such as refractive index (RI).

2. List of particles to be simulated.

3. List of processes to be simulated for a given particle list.

4. How the primary particles should be produced.

In our simulation, we want to obtain the angular distribution of Cherenkov light emitted by electrons travelling in the water. For that purpose, we create a sphere of 6 m radius filled with water. We use the same water refractive index as the function of photon wavelength as SNO+ in its simulation code (see [33] and references therein). We add electrons, optical photons, and γ - rays to the particle list. To the list of processes, we include relevant physics for electrons propagation: transportation, ionization, bremsstrahlung, and Cherenkov light production. On top of it, for electron's scattering, we add up one of the two mentioned scattering models: the default SNO+ MS model or the SS model. We do not define any physical processes for the optical photons except transportation, because we want to obtain light distribution as it is – not disturbed by other effects related to photon propagation. Electrons are injected at the point in the middle of the sphere along z-axis with energy E_e. Finally, we get the coordinates of the photons that have reached surface of the water sphere and save it to build the θ angular distribution. Figure 2.2 shows the geometry and an example event.We run two series of the simulations, first with the SS model and second with the MS model, for different E_e from the range of 0.3 - 5 MeV, injecting 1000 electrons at a time. Figure 2.3 and table 2.1 show the difference between Cherenkov light angular distributions of several MeV electrons propagated with the MS and SS models.

Clearly, one can see that the default SNO+ MS model has a sharper peak for energies of electrons in range 0.3 - 1 MeV, with a smaller fraction of photons emitted into angle $> \pi/2$ (tail fraction) and a smaller full width half maximum of the peak (FWHM).

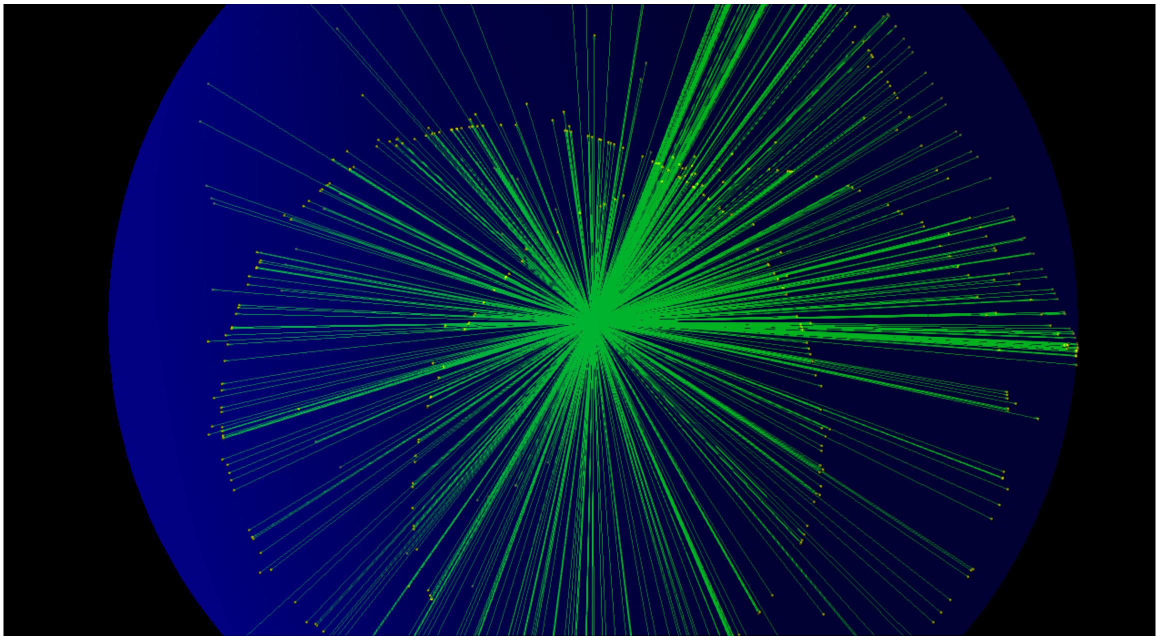

Figure 2.2: Blue water sphere with an electron injected in the middle. Green lines are trajectory of the emitted photons. One can see the pattern of Cherenkov ring on the surface of the sphere.

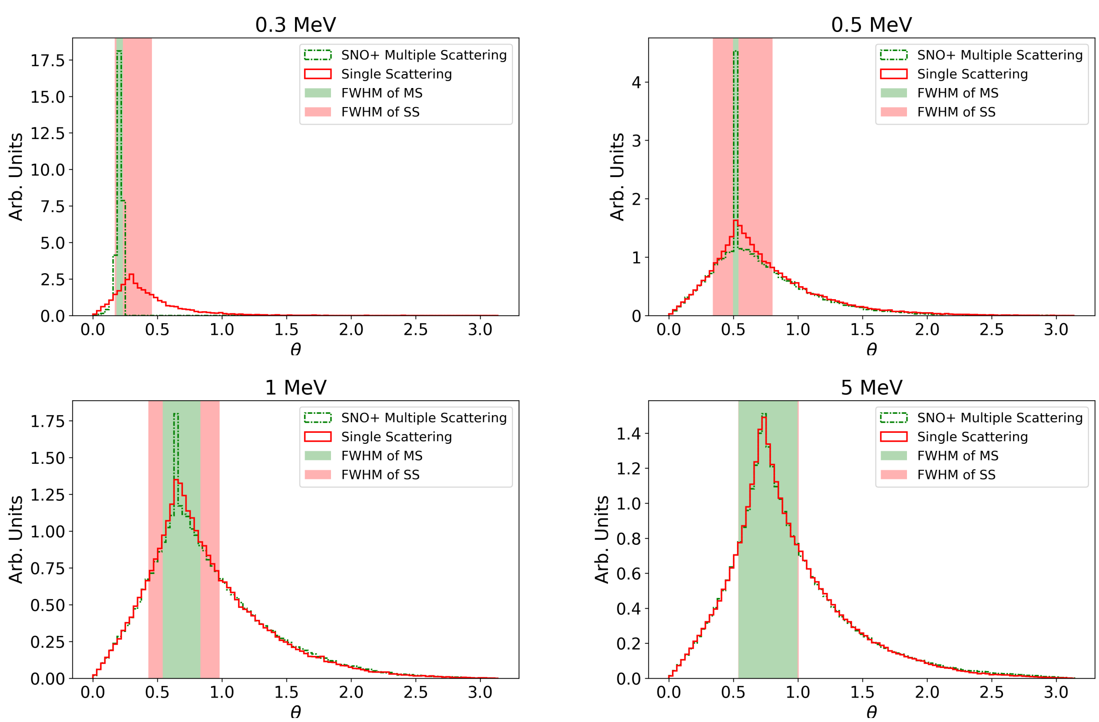

Figure 2.3: A comparison of Cherenkov light distributions obtained from using SS and SNO+ default MS models for electrons propagation as it would be observed in a spherical detector if we injected thousands of $E_e = 0.3$, 0.5, 1, 5 MeV electrons along the z-axis. The green and red regions specify FWHM zones for each distribution.

However, the distributions match much better at the energy of 5 MeV. This happens because Geant4 with the MS model for the electron propagation produces a large straight step for low energy electrons and emits most of the light into the Cherenkov angle with respect to this step. After that step electrons are either below or really close to the Cherenkov threshold energies and cannot emit more light. However, electrons propagated with the SS model have smooth trajectories with many scatterings (see fig. 2.4) and emit Cherenkov light along the whole track. At the higher energies, the electrons undergo enough steps, even with the MS model, and are able to emit light in different directions before they reach the Cherenkov threshold. Therefore, changing of the scattering model for electron propagation does highly influence the Cherenkov light emission. Since SNO+ data indicates that light withing events in data is more isotropic than the Geant4 prediction, the exact SS model can be further tested with SNO+ simulations and compared to the calibration data.

2.4 Cherenkov light coherence studies

The classical eq. (2.1) is obtained with the assumption that a charged particle travels in a straight infinite line with a constant speed [3, 23]. In reality, an electron that travels in a medium interacts with it and scatters many times while experiencing energy losses. As we described before, when Geant4 propagates a particle using MS models, it assumes some mean deviations from the trajectory with some $StepLength >$ mean free path of a particle and connects initial and final points of the step with a straight line. However, the real trajectory of the particle is a bent line with many more interactions points. Figure 2.4 demonstrates the difference between MS and SS models' trajectories for an electron traveling in water. To see how the electron scattering influences the assumed coherence, we calculate the Cherenkov angular distribution profile considering the physical origin of Cherenkov light as an interference effect, using the exact SS model for particle transportation.

Item	MS	SS	Coherent
0.3 MeV			
Peak position	0.21 ± 0.03	0.31 ± 0.03	0.29 ± 0.03
FWHM	$0.05^{+0.06}_{-0.05}$	0.29 ± 0.06	0.25 ± 0.06
Tail fraction	0.0001 ± 6e-5	0.0051 ± 0.0004	0.0083 ± 0.0006
0.5 MeV			
Peak position	0.52 ± 0.03	0.57 ± 0.03	0.57 ± 0.03
FWHM	$0.04^{+0.06}_{-0.04}$	0.46 ± 0.06	0.46 ± 0.06
Tail fraction	0.036 ± 0.002	0.045 ± 0.002	0.040 ± 0.002
1 MeV			
Peak position	0.69 ± 0.03	0.71 ± 0.03	0.71 ± 0.03
FWHM	0.29 ± 0.06	0.55 ± 0.06	0.59 ± 0.06
Tail fraction	0.089 ± 0.001	0.081 ± 0.001	0.084 ± 0.001
5 MeV			
Peak position	0.77 ± 0.03	0.77 ± 0.03	0.78 ± 0.03
FWHM	0.46 ± 0.06	0.47 ± 0.06	0.50 ± 0.06
Tail fraction	0.099 ± 0.001	0.092 ± 0.001	0.092 ± 0.001

Table 2.1: Detailed comparison of the distributions from fig. 2.3 and fig. 2.5.

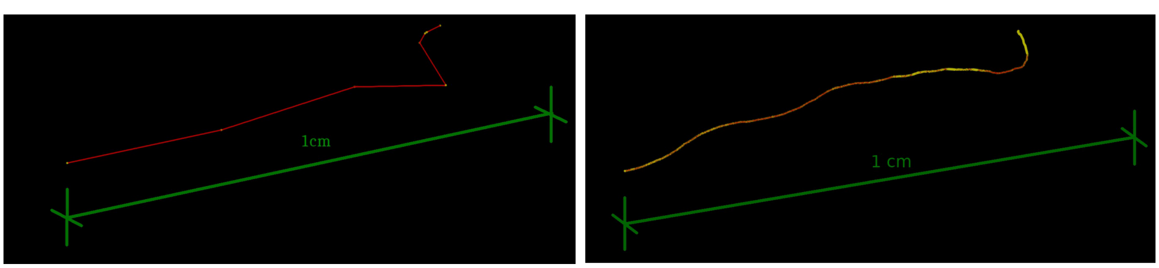

Figure 2.4: MS (left) and SS (right) simulated electrons trajectories for 2 MeV electrons in the water.

2.4.1 Taking into account interference between segments

First, we need to derive an appropriate expression that we will use to calculate the emitted Cherenkov light. In this section, we closely follow a SNO internal note of R.J. Komar [34] as well as derivations of Schiff [35] and Dedrick [36].

Schiff starts with defining the current density of a point charge e that starts moving with a constant speed v along z-axis at $t = 0$ and at $\mathbf{r} = 0$ is:

$$J_x(\boldsymbol{r}, t) = J_y(\boldsymbol{r}, t) = 0 \tag{2.9}$$

$$J_z(\boldsymbol{r}, t) = ev\delta(x)\delta(y)\delta(z - vt) \tag{2.10}$$

To calculate the angular distribution of the Cherenkov radiation, they use the exact expression for the average energy radiated at position $\boldsymbol{r}$ by a harmonically time-varying current distribution in a homogeneous isotropic dielectric medium [36]:

$$P_{k\omega}(\boldsymbol{r}) = \frac{nk^2}{2\pi r^2 c}|\int J_{\perp k}(\boldsymbol{r'})exp(-in\boldsymbol{k}\cdot\boldsymbol{r'})d\tau'|^2, \tag{2.11}$$

where $P_{k\omega}$ is the energy flow per unit area and angular frequency in the direction of observation (parallel to $\boldsymbol{k}$ or $\boldsymbol{r}$), $|\boldsymbol{k}| = \omega/c$, n is the index of refraction for the medium, and $J_{\perp k}$ is the component of the current density perpendicular to $\boldsymbol{k}$. Then they replace the density in eq. (2.10) by the Fourier amplitude of angular frequency ω

$$J_{z\omega}(\boldsymbol{r}, t) = \frac{e}{2\pi}\delta(x)\delta(y)\exp\left(iwz/v\right) \tag{2.12}$$

and put $J_{\perp k} = J_{z\omega}\sin\theta$ into eq. (2.11). Thereby, they get the energy flow per unit area and angular frequency

$$2\pi P_{k\omega}(\boldsymbol{r}) = \frac{ne^2\omega^2\sin^2\theta}{4\pi^2 r^2 c^3}|\int(exp(-i\omega z'(\frac{1}{v} - \frac{n\cos\theta}{c})dz'|^2. \tag{2.13}$$

For a pathlength L centered on the origin, the integral is evaluated to be

$$\int_{-L/2}^{L/2} e^{-i\omega z'(\frac{1}{v}-\frac{n\cos\theta}{c})}dz' = \frac{2\sin\left[\frac{\omega L}{2}(\frac{1}{v}-\frac{n\cos\theta}{c})\right]}{\omega(\frac{1}{v}-\frac{n\cos\theta}{c})}. \tag{2.14}$$

This is the definition of the delta function in the limit of $L \to \infty$

$$\lim_{L\to\infty} \frac{2\sin\left[\frac{\omega L}{2}(\frac{1}{v}-\frac{n\cos\theta}{c})\right]}{\omega(\frac{1}{v}-\frac{n\cos\theta}{c})} = 2\pi\delta(\frac{1}{v}-\frac{n\cos\theta}{c}), \tag{2.15}$$

which leads to the classical expression eq. (2.1).

As the result, from eq. (2.13) the radiated power is proportional to:

$$L^2\sin^2\theta\frac{\sin^2\chi}{\chi^2} \text{ and } \chi = \frac{\omega L}{2}(\frac{1}{v}-\frac{n\cos\theta}{c}) \equiv \frac{\pi L}{\lambda'}(\frac{1}{n\beta}-\cos\theta), \tag{2.16}$$

where $\lambda' = 2\pi c/n\omega$ is the wavelength in the medium. The behaviour of (eqn. 2.16) is different for small and large L. For $L \gg \lambda'$, the angular distribution is sharply peaked at the Cherenkov angle θ_0 and has a full width at half maximum

$$\delta\theta \simeq \frac{\lambda'}{L\sin\theta_0}.$$

However, when the pathlength decreases and $L \ll \lambda'$, the $\sin^2\chi/\chi^2$ becomes constant and the radiation is emitted over a dipole angular distribution.

To estimate ratio between the straight pathlength of a charged particle and wavelength of emitted light to achieve full light output on a segment, they integrate over the angular distribution eq. (2.16). The integral over $\sin^2\chi/\chi^2$ goes to π when χ limits approaching $\pm\infty$. However, most of the integral value lays between $\chi = \pm\pi$. Therefore from eq. (2.16), we get the conditions on the pathlength to preserve a high level of coherence

$$\left|\frac{L}{\lambda'}(\frac{1}{n\beta}\pm 1)\right| > 1, \tag{2.17}$$

which, for $\beta = 1$ and $n = 4/3$, becomes

$$L > 4\lambda' \tag{2.18}$$

PMTs are able to detect light with the wavelengths up to $\lambda = 720$nm. Hence, we need straight pathlengths $L \approx 3\mu m$ to get full coherence. From the SS model we used, the mean free path between scattering of electrons in the water is $\approx 1.3\mu$m (see fig. 3.9), which is at the same order as our estimate of the minimal L.

To consider interactions between small segments of a track, we will use the formulae developed by Dedrick [36]. Equation (2.11) transforms into a sum of integrals over each straight path segment ν

$$P_{k\omega}(\boldsymbol{r}) = \frac{nk^2}{2\pi r^2 c} |\sum_{\nu=1}^{N} I_\nu|^2, \tag{2.19}$$

where

$$I_\nu = \frac{e}{2\pi} \sin\Theta_\nu e^{i(\delta_\nu + \chi_\nu)} l_\nu \frac{\sin\chi_\nu}{i\chi_\nu} \tag{2.20}$$

and the phase angles are given by

$$\chi_\nu = \frac{\omega l_\nu}{2}(\frac{1}{v_\nu} - \frac{n}{c}\cos\Theta_\nu) \equiv \frac{\pi l_\nu}{\lambda'}(\frac{1}{n\beta_\nu} - \cos\Theta_\nu), \tag{2.21}$$

$$\delta_\nu = \omega t_\nu - nk(x_\nu \sin\theta\cos\varphi + y_\nu \sin\theta\sin\varphi + z_\nu\cos\theta). \tag{2.22}$$

Now, the expression for the total energy radiated is composed not only from terms of the form $I_\nu I_\nu^*$ but also $(I_\nu I_\mu^* + I_\nu^* I_\mu)$ that represent interference effects between segments.

Equation (2.19) can be conveniently applied to a step-based Monte-Carlo simulation to calculate the total angular distribution of Cherenkov light. Hence, we decided to make a hybrid simulation of Cherenkov light emission using the radiation model described above and Geant4 using the SS model for electron transportation. The difference from the algorithm described in Section 2.1 is that now we get the power of emitted Cherenkov light from a track as the whole instead of considering simulation steps independently.

2.4.2 Geant4 setup and integration

To propagate the electrons, we use the same Geant4 geometry setup as described in Section 2.3, but only with the SS model for propagation of electrons. However, instead of getting information about emitted photons, we record each electron's position, time, and $\beta = v/c$ at each step point. We run each simulation with 1000 electrons with the initial energies E_0 = 0.3, 0.5, 1, 5 MeV. We use the stored trajectories to calculate the sum of the integrals I_ν (2.20) for $\lambda = 400$nm. As a result of the calculations, we obtain angular dependence of the Cherenkov light power as it would be observed in a spherical detector.

2.4.3 Comparing to the default light emission simulation

Since we calculate power distribution only for a single wavelength, we have to change the Geant4 setup described in Section 2.3 and make it emit photons of the single wavelength $\lambda = 400$nm. Then, we run simulations with 1000 electrons with the initial energies E_0 = 0.3, 0.5, 1, 5 MeV. Figure 2.5 and table 2.1 show the result of the simulations.

The simulation with the default SNO+ MS model for particle propagation has a more noticeable difference from the SS model with the default light emission method than the model that takes into account interference effects. Therefore, we will be using the SS model with the default light emission as the reference since it has minimal deviations from the more physically accurate one and is already implemented in Geant4.

2.5 Conclusions

There are significant differences in Cherenkov light distribution emitted by electrons using multiple (MS) and single scattering (SS) models that we discussed in Section 2.4.3 and in the end of Section 2.3. The more physically accurate calculations, which take into

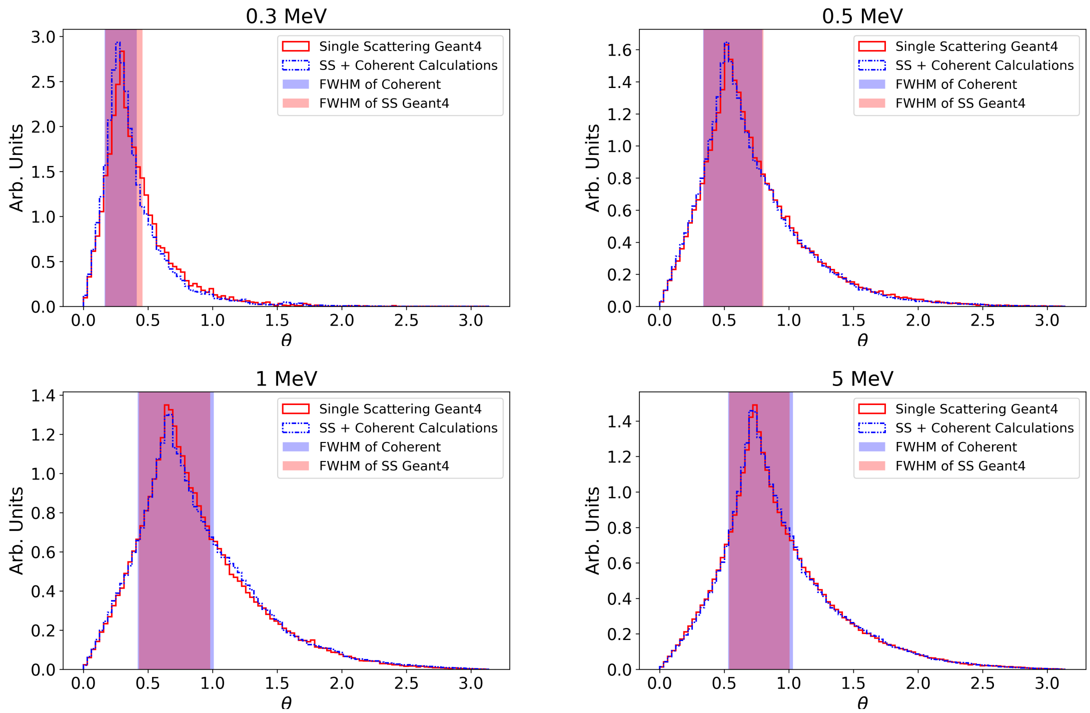

Figure 2.5: A comparison of simulated Cherenkov light distributions emitted by an electron moving in the water as it would be observed in a spherical detector if we injected thousands of several MeV electrons along the z-axis. We use default Geant4 light emission method (red line) and light emission that takes into account interference effects between track segments (blue line). The energy of the electrons is specified on each subplot.

account the interference nature of Cherenkov light radiation, have minimal deviations from the current simulation tools with the SS model for electrons propagation (MS is used by default in SNO+). The results are also in agreement with the studies on "Effects of electron scattering on Cherenkov light output" by M.G.Bowler [37], where the authors studied if the coherence violation due to electron scattering can cause a decrease in Cherenkov light output in the water. Therefore, for the propagation of electrons of several MeV energies in the water, one can use Geant4 approximation for Cherenkov photons emission. However, we need to change the scattering model from the default SNO+ MS to SS and explore the effects of the changes on the data.

Chapter 3

Corrections to Cherenkov model in SNO+ simulations

As we concluded in the previous chapter, the single scattering model has to be used instead of the default SNO+ multiple scattering model for the simulation of electron with energy up to 5 MeV propagation in the water in order to make it more physically accurate. By doing this, we can estimate the effect of changing the scattering model by comparing the modified SNO+ MC simulation to the existing one and to SNO+ calibration data.

3.1 SNO+ and Calibration data

SNO+ (Sudbury Neutrino Observatory) experiment [38] is an ongoing low-background neutrino experiment tailored for the detection of MeV energy depositions. The experiment has several stages, including a water phase where the detection volume consisted of water and Cherenkov light was used to detect neutrinos. To describe an event in the water phase, SNO+ uses Cherenkov light position and arrival time to infer the characteristics of the particle that has created the light. The data for this work comes from the water phase only.

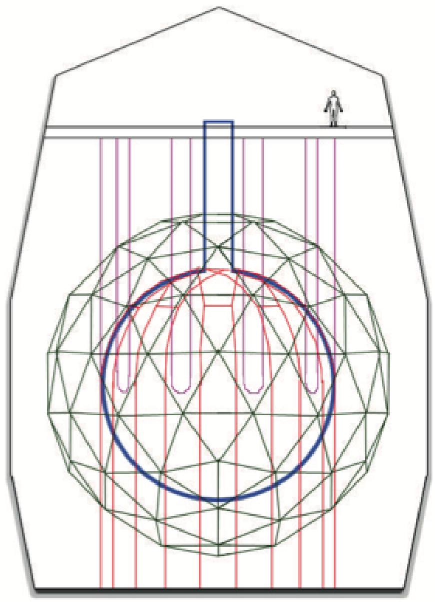

Figure 3.1: SNO+ schematics from [40]. 6 m radius acrylic vessel (blue) surrounded by support structure (green) and is held by ropes (pink). Ropes pictured in red are used in the scintillator phase to compensate buoyancy of the AV filled with scintillator.

3.1.1 SNO+

SNO+ is the successor of the SNO experiment [39] and inherits most of its infrastructure. The detector consists of a spherical 6 m-radius acrylic vessel (AV) filled with about 900 tonnes of pure water for the water phase. It is surrounded by 9,394 inward looking photomultiplier tubes (PMTs) that give about 50% photo coverage. The PMTs are mounted on a support structure around the AV with an average radius of 8.4m. The cavity where the detector is installed is also filled with water to decrease backgrounds from natural radioactivity of rocks, PMTs, and auxiliary structures. To decrease the muon, a long lived charged particle, background, SNO+ is built about 6,000 m of water equivalent depth under the ground. There are also 90 outward looking PMTs located on the support structure that help to detect and reject atmosphere muons. Figure 3.1 shows the schematics of the detector.

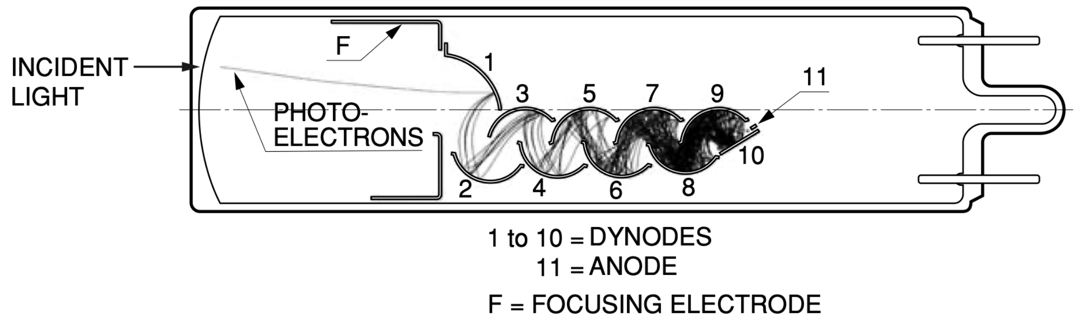

Figure 3.2: An example of a dynode system operation from [41]. There is an electrical potential difference between each dynode. First, a photoelectron hits the first dynode and makes several more electrons escape the dynode. Then, these escaped electrons travel to the next dynode and get multiplied. It repeats until the multiplied charge reaches the final dynode – anode and gets collected.

3.1.2 SNO+ water phase events

The detection of the neutrinos in the water phase of the SNO+ detector happens through the observation of Cherenkov light. A photon hitting a PMT may create a photoelectron with the probability that depends on quantum efficiency of the photocathode. Then, the photoelectron is accelerated to the dynode system and gets multiplied by secondary emission (see fig. 3.2); creating an output signal. The signal is recorded with the information about a PMT, which has detected the signal, and a timestamp. This data forms a PMT hit and a set of PMT hits recorded in a specified time window after each valid set of conditions on detection (global trigger) is called an event. Figure 3.3 shows an example Cherenkov ring event on a SNO+ event display. Every event is characterized by position vertex, direction, energy, and isotropy. The position vertex is determined based on the time difference between PMTs signals. The direction is calculated by the angular distribution of the PMT hits. The energy is proportional to the number of PMT hits within an event [42]. The event isotropy, which is an important concept for this thesis, will be discussed briefly in a following section.

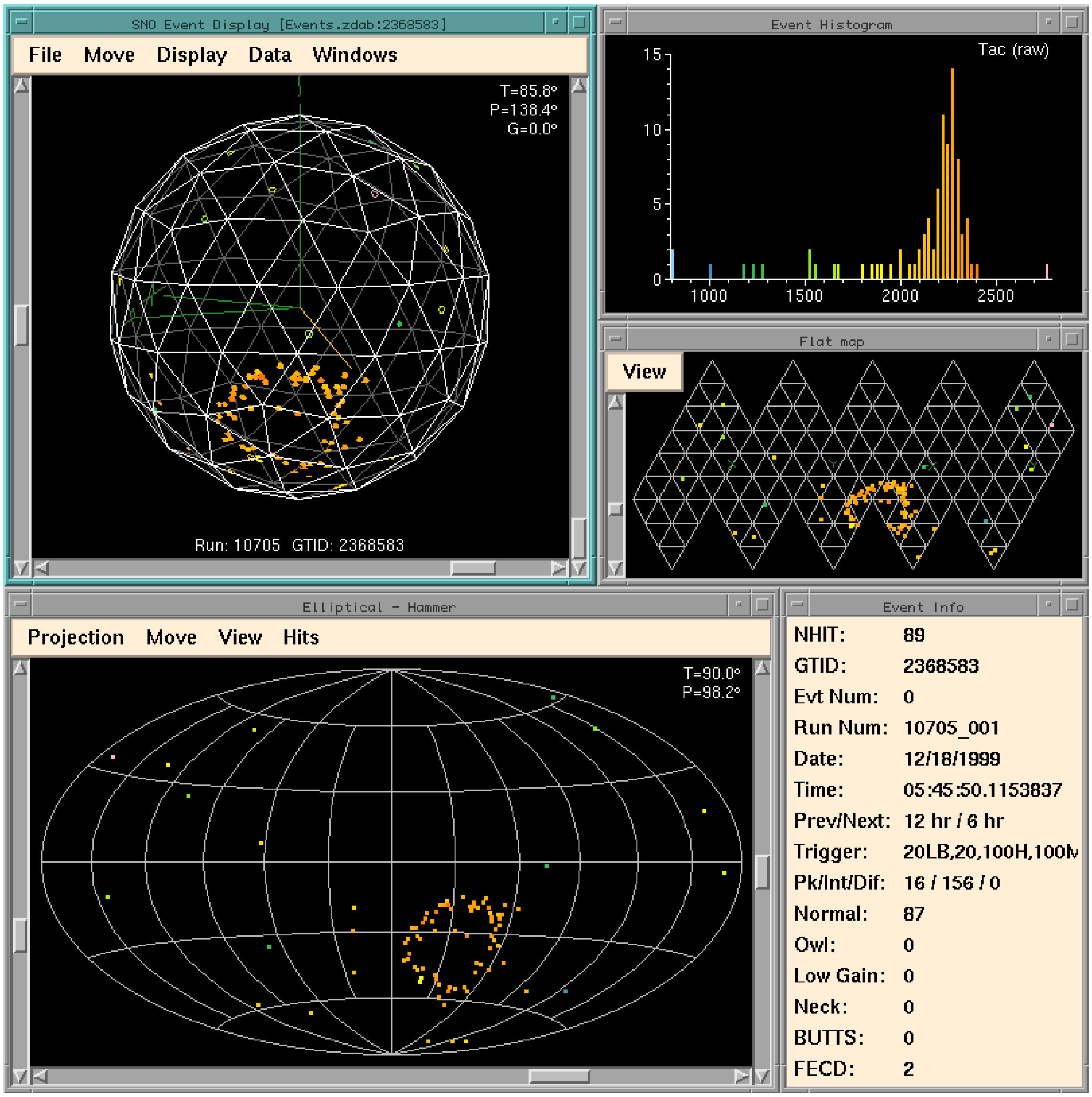

Figure 3.3: An example of a neutrino candidate event with a Cherenkov ring in SNO. Event display shows the PMTs that detected the light in different projections. The histogram shows the time distribution of the PMT hits and the colour of the hit codes the time of the light arrival.

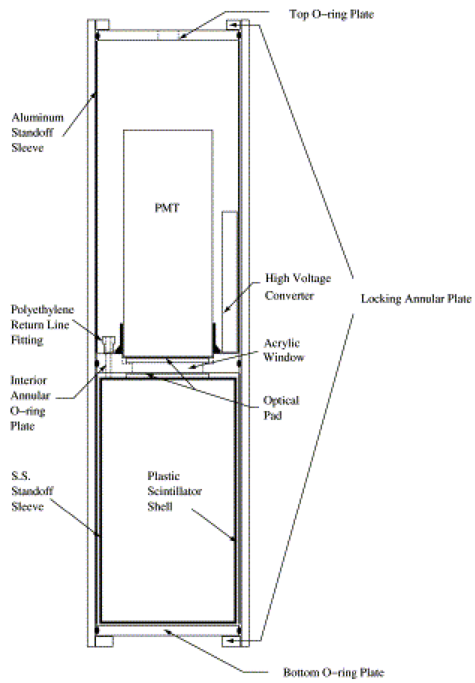

Figure 3.4: The ^{16}N decay chamber schematics. The ^{16}N decays occur in the bottom region, bounded by 3 mm of a cylindrical shell of plastic scintillator. The upper volume contains a PMT that detects scintillator light. Taken from [44].

3.1.3 SNO+ Monte Carlo

In SNO+, the simulation is handled by Geant4 [22] also using GLG4sim, a package for precise scintillator light simulations [43]. The detector geometry is accurately reproduced in the simulation. Generators allow the injection of selected particles in an arbitrary spot, with specified kinematics and timestamps. When the particles are generated, Geant4 propagates them through the detector volume and simulates any physical processes, such as Cherenkov light emission, scattering, absorption, and PMT response. Finally, front-end electronics, trigger system and event builder are simulated [40]. Detector conditions for each physical run – such as date, PMT and electronics calibrations, trigger conditions – are stored in a detector database. Therefore, one can simulate the Monte-Carlo data that corresponds to specific conditions and this simulated data can be analyzed the same way as the real data.

3.1.4 ^{16}N and AmBe calibration sources

The detector is planned to undergo calibrations during its lifetime to make sure it works properly and measurements are accurate. To conduct calibrations that depend on the detected particle energy, SNO+ uses ^{16}N [44] and AmBe [45] radioactive sources.

The ^{16}N is produced via the (n,p) reaction on ^{16}O of CO_2. It provides nearly monoenergetic 6.13 MeV γ-rays that follow the β-decays of ^{16}N. The γ-ray Compton scatters producing electrons of roughly 5 MeV energy that emit Cherenkov light within the detector. The source is placed into an enclosure (see fig. 3.4), which includes plastic scintillator that captures the electron from the β-decay. The scintillation signal is picked up by a PMT installed inside the enclosure. This signal is used as an internal tag for an ^{16}N event and allows easy calibration event identification.

The ^{241}Am^{9}Be is a neutron source. ^{241}Am emits an α-particle that may be absorbed by ^{9}Be target, which then will decay into ^{12}C through neutron emission. ^{12}C is produced in an excited state and immediately de-excites by emitting a 4.4 MeV γ-ray. The neutron thermalizes and gets captured by a proton within the medium in about 200μs producing 2.2 MeV γ. Therefore, the AmBe source creates 2 consecutive events, referred to as prompt (4.4 MeV γ) and delayed (2.2 MeV γ). The coincidence in a specified time window makes it possible to identify these calibration events.

3.1.5 Isotropy and the β_{14} parameter

In the water phase, the projection of Cherenkov light on PMTs is expected to have a well defined circle shape with a high degree of anisotropy, but the average number of PMT hits in an event is $\sim$9 hits/MeV of energy of a charged particle. It is therefore hard to distinguish different signatures of Cherenkov cones smeared by electron scattering and identify the origin of an event. To overcome this, we can quantitatively characterize the isotropy of the light within an event using the angular distribution of PMTs with hits. Figure 3.5 shows a schematic representation of PMT hits in a Cherenkov ring event and quantities that we define. Here $\mathbf{r}_i$ and $\mathbf{r}_j$ are vectors that

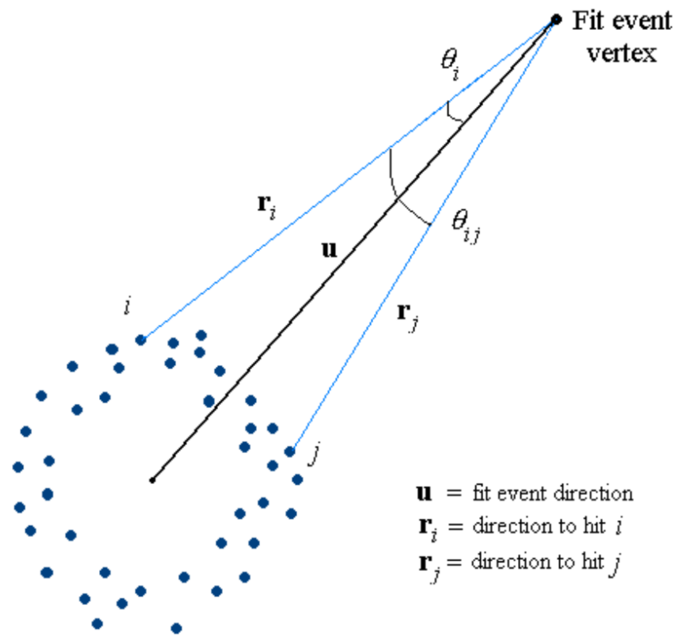

Figure 3.5: The image is taken from [42]. It explains θ_{ij} angles within Cherenkov ring event.

connect fit vertex with i-th and j-th PMT hits respectively and $\mathbf{u}$ is the normalized fit direction. With these quantities, we can define θ_{ij} that is the angle between $\mathbf{r}_i$ and $\mathbf{r}_j$, so $\cos\theta_{ij} = \frac{\mathbf{r}_i \mathbf{r}_j}{|\mathbf{r}_i||\mathbf{r}_j|}$.

We introduce β_l parameters that are invariant to rotations and give information about the spatial distribution of hits within the event

$$\beta_l = \frac{2}{N(N-1)} \left[\sum_{i=1}^{N-1} \sum_{j=i+1}^{N} P_l(\cos\theta_{ij}) \right], \tag{3.1}$$

where N is number of hits in the event and P_l is Legendre polynomial. From [42] we know that the best separation between different events signatures is achieved by using $\beta_{14} = \beta_1 + 4\beta_4$ parameter. For example, Figure 3.6 shows β_{14} distributions of two naturally occurring radioactive isotopes ^{214}Bi and ^{208}Tl. The distributions have different characteristics, like position of the peak and width, and therefore can be separated using β_{14}. In the event with higher isotropy, we expect the light angular

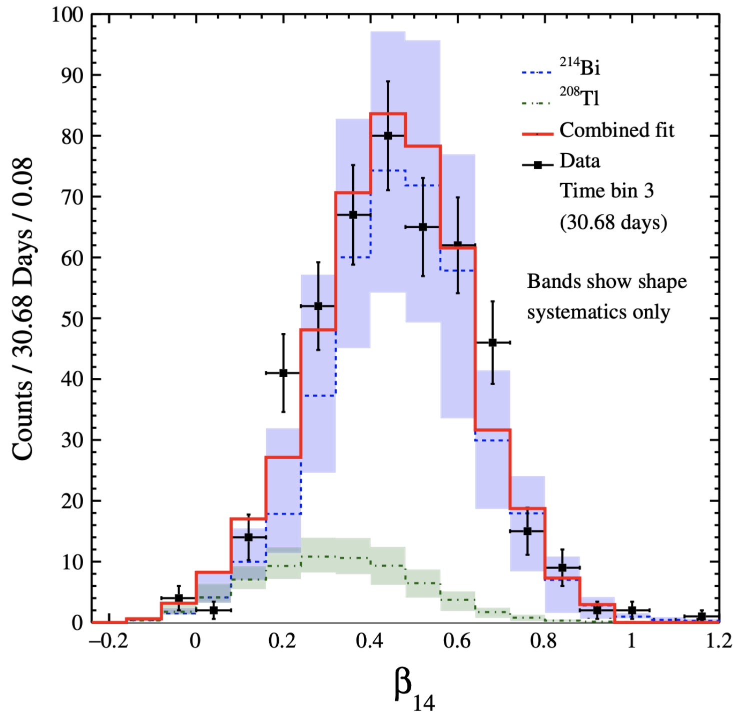

Figure 3.6: The image is taken from [46]. Data and MC β_{14} distributions of ^{214}Bi and ^{208}Tl decays. These decays are distinguished by β_{14}.

distribution to be broader.

3.1.6 β_{14} discrepancy in SNO+

The β_{14} is a useful parameter for event selection, however, during the calibration phase a discrepancy between data and Monte-Carlo was found [47]. Figure 3.7(left) shows the difference in β_{14} distributions for ^{16}N source simulation and data. The data has a lower mean value of the parameter, which means it has a higher degree of isotropy. Figure 3.7(right) demonstrates an attempt to fix the difference by smearing the Cherenkov emission angle, increasing the isotropy of the event. It helps to match mean values for ^{16}N data, but it doesn't match β_{14} for lower energy calibration sources.

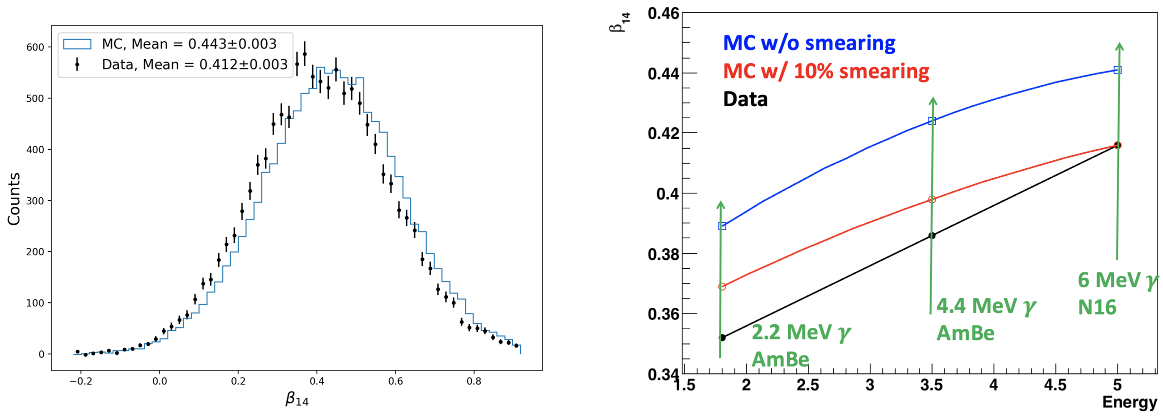

Figure 3.7: Discrepancy between data and MC of ^{16}N source adapted from [47] (left). Discrepancy in mean values of β_{14} of ^{16}N and AmBe sources (right) with an attempt to fix it by smearing the Cherenkov emission angle [48].

3.2 Implementing SS sampling within Geant4

From the β_{14} discrepancy, we know that data has a higher degree of isotropy than the default SNO+ Monte-Carlo. From the previous chapter, we also know that switching to the single scattering model for electron propagation makes the total Cherenkov light angular distribution more broad, increasing FWHM as was shown on fig. 2.3. Therefore, we want to use the single scattering model in SNO+ MC. However, the direct usage of the SS model for electron propagation within SNO+ simulations faces several challenges. Firstly, SNO+ uses software with a deprecated Geant4 version (10.0.0p3) that does not have the same SS model implementation for low energy electrons as the new Geant4 versions – therefore, we cannot explicitly use the model. Secondly, as described in Section 2.2, the SS model is significantly more computationally expensive than MS models. A comparison of run time of Geant4 simulations with electrons propagation using the default SNO+ MS model and SS model shows that the latter takes about 7 times longer. That means we cannot afford to use it for generating large MC samples needed for analysis, which contain millions of simulated electrons trajectories. In order to overcome these limitations, we modify the Geant4 Cherenkov light injection model in a way that the total Cherenkov light distribution corresponds

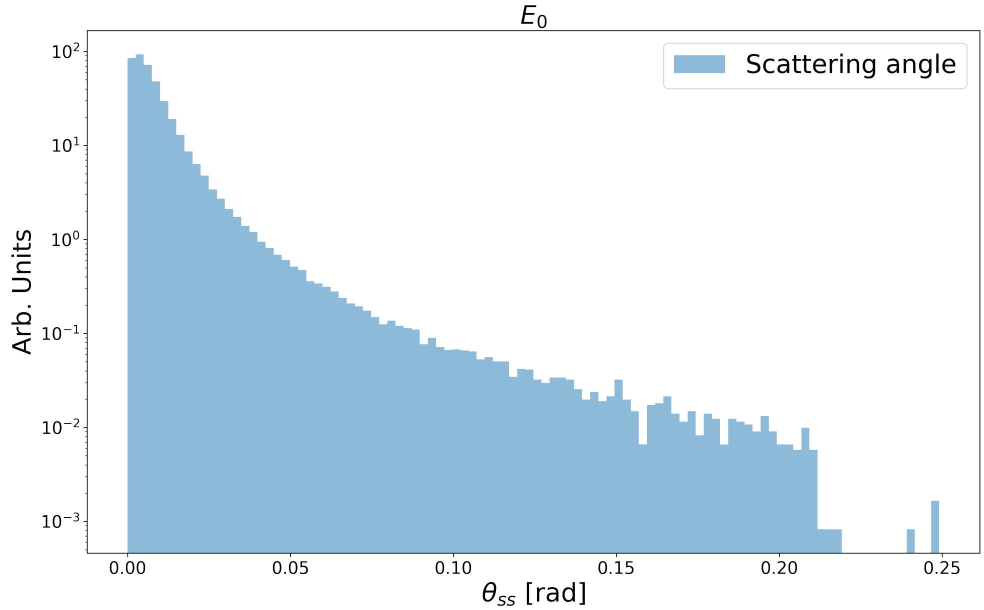

Figure 3.8: An example of θ_{ss} distribution for 1 MeV energy electron.

to the one obtained by using the SS model for electron propagation. Further in the text, this model will be referred to as "Cherenkov light sampling".

3.2.1 Scattered angle and free mean path distributions

To implement the algorithm we first need to know the scattering angle of an electron $\theta_{ss} = \theta_{ss}(E_e)$ and the free mean path of the electron $\lambda_{ss} = \lambda_{ss}(E_e)$ as the functions of the electron's energy. Since we want the sampling to work fast, we do not use the exact calculations of the cross-section as described in Section 2.2. We know, a priori, that electrons in the SNO+ simulation are propagated in the water. We also know from Chapter 2 that usage of the SS model produces different Cherenkov light distribution at the energy scale of electron from few MeV up to approximately 5 MeV. We use this knowledge and build distributions of $\theta_{ss}(E_e)$ (see fig. 3.8) with a step of 50 keV and $\lambda_{ss}(E_e)$ (see fig. 3.9) with a step of 100 keV, where the step sizes are an arbitrary choice, for electrons travelling in water with energies from 0.3 MeV to 6 MeV.

We obtain these distributions numerically by running a Geant4 simulation. Similarly

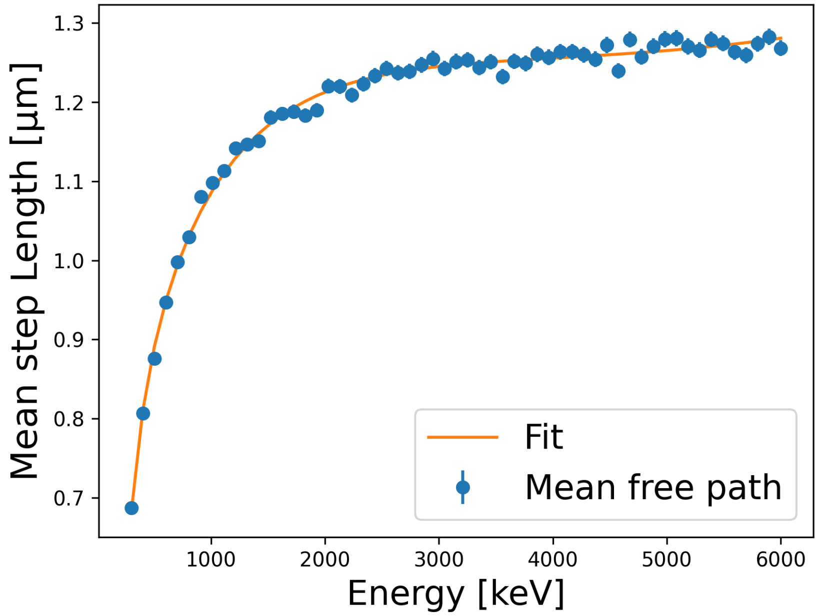

Figure 3.9: Fitted $\lambda_{ss}(E_e)$ distribution.

to the simulation construction described in Section 2.3, we have to define geometry, processes and particles lists. The lists include only electrons and the SS model, as well as transportation for the particle propagation. The geometry is a 5×5 cm cube of water so electrons with energy of few MeV, which are injected in the centre of cube, deposit a negligible amount of energy before escaping the volume and are no longer being tracked. We run the simulation injecting several thousand electrons and record the scattering angle θ_{ss} after each interaction (see fig. 3.10) and a step length until they leave water volume. We run several simulations for different energies in the range from 0.3 MeV to 6 MeV and find the average of obtained step lengths to get λ_{ss} for the specified energy (see fig. 3.9). To find λ_{ss} as a smooth function of energy, we use the model described in Section 2.2 and fit it to the data. $\lambda_{ss}(E) \sim 1/\sigma(E)$, where $\sigma(E)$ is total cross-section of single scattering. Combining this with eq. (2.4) we obtain an energy dependence of λ_{ss}:

Coefficient	Value	Uncertainty
κ_1	2.45e+05	0.33e+05
κ_2	-2.94e+04	0.31e+04
κ_2	1.26e+03	0.72e+03
κ_4	4.14e-05	0.36e-05
κ_5	-1.33e-02	0.11e-02
κ_6	1.14e-02	0.03e-02

Table 3.1: Coefficients of eq. (3.2) obtained after fit to the data.

$$\lambda_{ss}(E) \sim 1/\sigma(E) = \frac{E^2}{\sum_{k=1}^{6} \kappa_k E^{\frac{k-1}{2}}}, \tag{3.2}$$

where κ_k are free parameters. After the fit (see fig. 3.9) we get the values of κ_k coefficients, which are listed in table 3.1. We also interpolate $\theta_{ss}(E_e)$ distributions by nearest-neighbour interpolation.

3.2.2 Cherenkov light sampling

As was mentioned in Section 2.1, Cherenkov photons are emitted with respect to the direction of particle movement $\vec{p}_0$. This is a momentum vector in the starting point of the step or difference between the coordinates of the end point of the step and the starting point of the step normalized to one. To reproduce the SS model Cherenkov light distribution we sample $\Delta\theta$ from $\theta_{ss}(E_e)$ distribution by inverse transform sampling and change $\vec{p_0}$ by $\Delta\vec{p_0}(\Delta\theta)$. We do this N_θ times and emit a photon in the Cherenkov angle with respect to a new $\vec{p}_0$ (see fig. 3.11). We repeat these steps $\langle n \rangle$ times until all photons from the step are emitted. After the mean number of photons per steps $\langle n \rangle$ is calculated, the new algorithm is as follows:

(1.) Divide a step i into sub-steps of an average length required to emit one photon $LengthPerPhoton = \frac{StepLength}{\langle n \rangle}$.

(2.) Calculate the mean energy of the particle on a sub-step E_{ij}, where i is step number and $j = [1, \langle n \rangle]$ is sub-step number. $E_{ij} = E_i - (j - \frac{1}{2})\frac{E_i - E_{i+1}}{\langle n \rangle}$.

(3.) For the sub-step j calculate number of scatterings $N_\theta = \frac{LengthPerPhoton}{\lambda_{ss}(E_{ij})}$

(4.) Sample $\Delta\theta$ from $\theta_{ss}(E_{ij})$ and build a unit momentum displacement vector $\Delta\vec{p}_0 = (1; \Delta\theta; \Delta\varphi)$, where $\Delta\varphi$ is a random value from 0 to 2π. Then change the direction of $\vec{p}_0$ by $\Delta\vec{p}_0$.

(5.) Repeat (4.) N_θ times and then emit a photon to Cherenkov angle θ_C with respect to $\vec{p}_0$

(6.) Repeat (2.) - (5.) for all sub-steps, so j goes through values from 1 to $\langle n \rangle$.

(7.) Record the last value of $\vec{p}_0$ after the last sub-step in a step.

(8.) Repeat (1.) - (7.) for the next $i+1$ simulation step starting with $\vec{p}_0$ value obtained in the end of the previous i step.

3.2.3 Comparing MS model with sampling to SS model

To assess how accurate sampling reproduces Cherenkov light distribution obtained with the SS model for electron propagation, we conduct MC simulations as described in Section 2.1. Geant4 was modified to use a new Cherenkov light generation algorithm, described in Section 3.2.2, to the simulation with the default SNO+ MS model. Figure 3.12 and table 3.2 demonstrate and characterize obtained distributions.

One can see that the light distribution obtained with the Cherenkov light sampling is different from the SS model with the default light emission method. The biggest difference is for electrons of 0.3 MeV energy and, again, the difference for 5 MeV becomes negligibly small. However, the 0.3 MeV electrons have small light output and do not contribute much to the final light distribution. The simple benchmark mentioned in the beginning of Section 3.2 shows a 7% increase of computation time

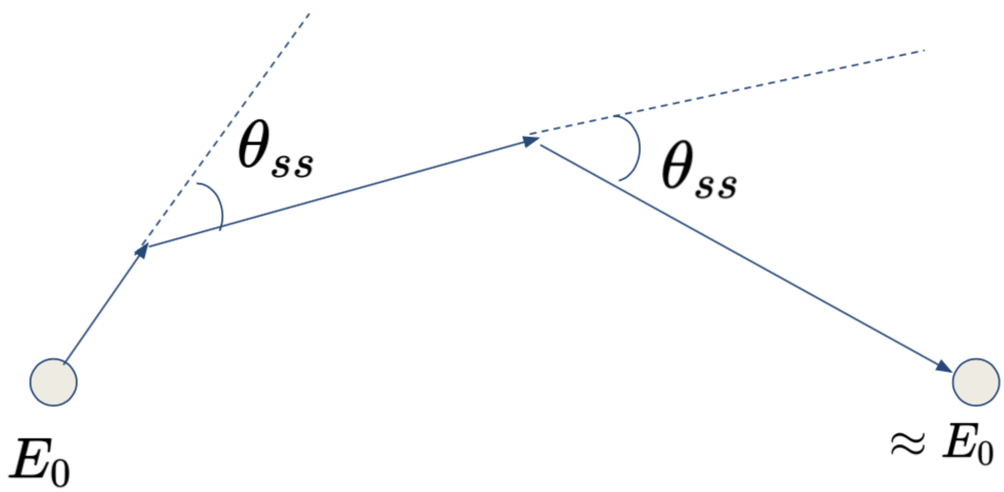

Figure 3.10: Schematics of θ_{ss} angles. First point is the point of the injection of electron with energy E_0. The solid arrows represent electron's steps. We record an angle of each scattering with respect to previous step. In the end when electron leaves the water volume it has energy approximately equal to the initial E_0.

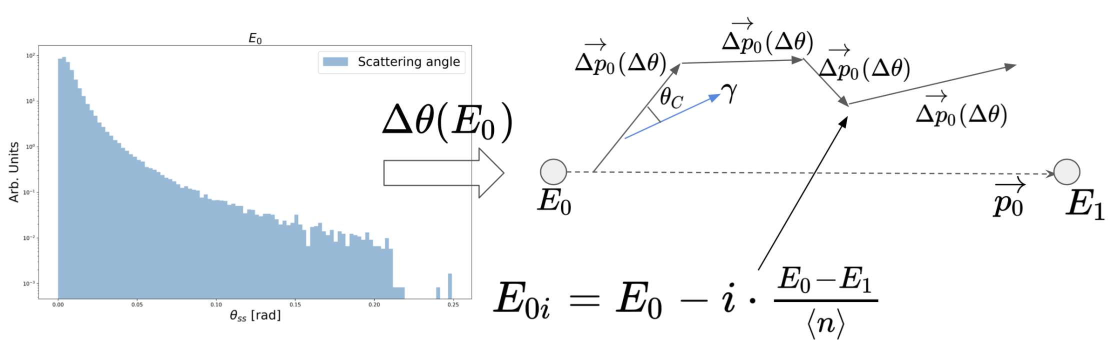

Figure 3.11: Process of Cherenkov light sampling by changing the direction with respect to which Cherenkov photons injection is happening.

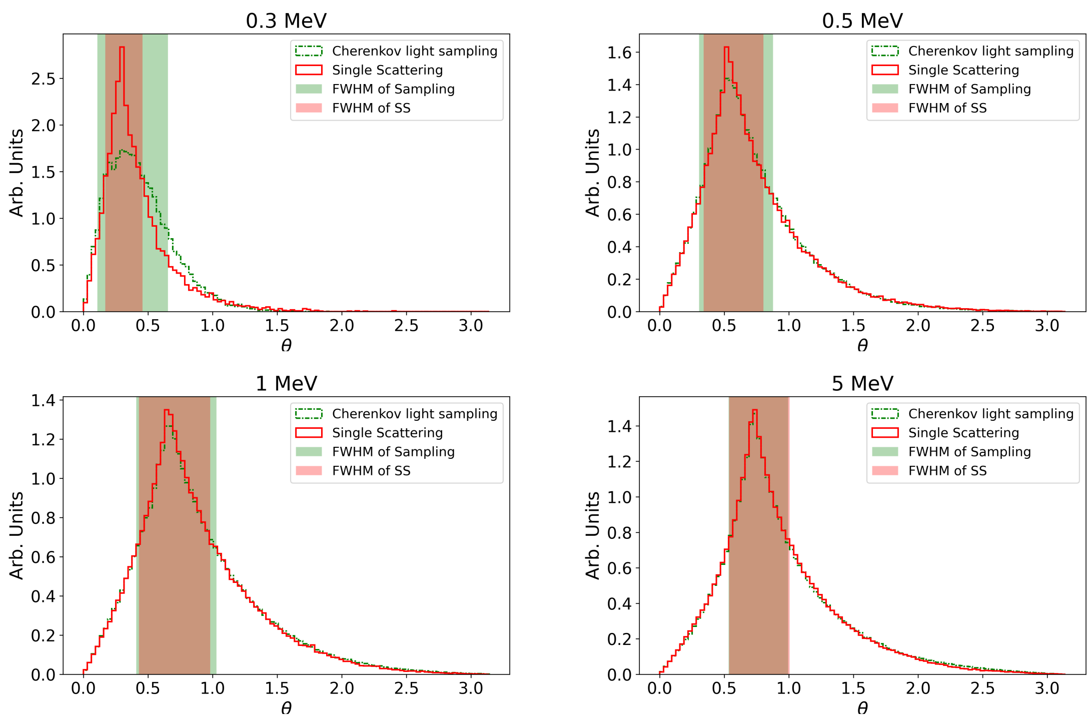

Figure 3.12: A comparison of simulated Cherenkov light distributions emitted by an electron moving in the water as it would be observed in a spherical detector if we injected thousands of electrons with 0.3, 0.5, 1, and 5MeV energies along the z-axis. Default Geant4 light emission method with the SS model (red line) and modified Cherenkov light emission with the default SNO+ MS model (green line). The energy of the electrons is specified on each subplot.

Item	MS	SS	Coherent	Sampling
		0.3 MeV		
Peak position	0.21 ± 0.03	0.31 ± 0.03	0.29 ± 0.03	0.38 ± 0.03
FWHM	$0.05^{+0.06}_{-0.05}$	0.29 ± 0.06	0.25 ± 0.06	0.55 ± 0.06
Tail fraction	0.0001 ± 6e-5	0.0051 ± 0.0004	0.0083 ± 0.0006	0.0054 ± 0.0004
		0.5 MeV		
Peak position	0.52 ± 0.03	0.57 ± 0.03	0.57 ± 0.03	0.59 ± 0.03
FWHM	$0.04^{+0.06}_{-0.04}$	0.46 ± 0.06	0.46 ± 0.06	0.57 ± 0.06
Tail fraction	0.036 ± 0.002	0.045 ± 0.002	0.040 ± 0.002	0.045 ± 0.002
		1 MeV		
Peak position	0.69 ± 0.03	0.71 ± 0.03	0.71 ± 0.03	0.72 ± 0.03
FWHM	0.29 ± 0.06	0.55 ± 0.06	0.59 ± 0.06	0.62 ± 0.06
Tail fraction	0.089 ± 0.001	0.081 ± 0.001	0.084 ± 0.001	0.090 ± 0.001
		5 MeV		
Peak position	0.77 ± 0.03	0.77 ± 0.03	0.78 ± 0.03	0.76 ± 0.03
FWHM	0.46 ± 0.06	0.47 ± 0.06	0.50 ± 0.06	0.46 ± 0.06
Tail fraction	0.099 ± 0.001	0.092 ± 0.001	0.092 ± 0.001	0.102 ± 0.001

Table 3.2: A complemented with Cherenkov light sampling model table 2.1 that characterizes distributions on fig. 2.3, fig. 2.5, and fig. 3.12.

comparing to the unmodified light emission, which is a more efficient solution than usage of the SS model for particle propagation that increases computational time by 700%. Therefore, we use this model and introduce an effective parameter to tune the model to the data, which is described in the next section.

3.2.4 Fitting the model to the SNO+ data

We develop the Cherenkov radiation model described in the previous sections considering the SS effect on Cherenkov light emission. However, it does not exactly reproduce the process and therefore it is an effective model. To complete the model we should tune it to the measured data. In Section 3.1.5 we introduced the β_{14} parameter. While

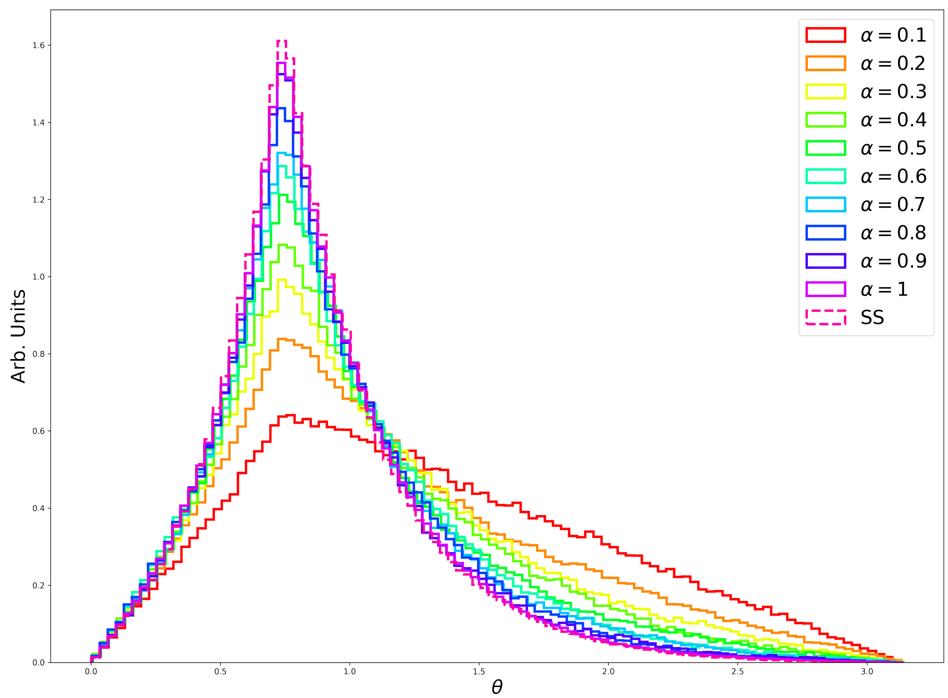

Figure 3.13: A comparison of simulated Cherenkov light distributions by Cherenkov light sampling with different α emitted by an electron moving in the water as it would be observed in a spherical detector if we injected thousands of 1 MeV electrons along the z-axis.

total angular distribution of Cherenkov light that we were comparing so far is the average quantity over all the events, β_{14} is sensitive to the way light is distributed within an event. Also, one of the goals of this thesis is fixing β_{14} discrepancy between data and MC. For that reason, to tune the model, we use calibration sources ^{16}N and AmBe (see Section 3.1.4) and fit its β_{14} mean values of the MC simulation with the new model for Cherenkov light emission to the β_{14} mean value of the calibration data. In order to do this, we introduce an effective parameter α that scales the mean free path of an electron in water $\lambda'_{ss}(E) = \alpha\lambda_{ss}(E)$. Changing this parameter will change the number of scatterings per Cherenkov photon and smear the resulting Cherenkov light angular distribution (see fig. 3.13).

We run simulations with different α in a range from 0.1 to 1 for ^{16}N and AmBe sources with the run numbers corresponding to the sources placed in the middle of the detector. For the ^{16}N events selection we require event to have a tag as described in Section 3.1.4. For the AmBe events selection, we require two consecutive events with the time difference of less than 200μs, time big enough for a neutron capture to happen but small enough to not pick up a lot of background, and distance of less than 1m between the event vertices. The run numbers for corresponding data and detailed selection criteria for data and MC one can find in appendix B. As the result we obtain β_{14} as the function of α for 3 different energies of γ - rays. Figure 3.14 shows that to match the data α should be chosen in between 0.5 and 0.6. Therefore, we fit $\beta_{14}(\alpha)$ for each γ-ray energy with $\beta_{14}(\alpha) = a\sqrt{\alpha} + b$ in the specified range. To find an optimal value of α, we then minimize the function:

$$\chi^2(\alpha) = \sum_i \frac{(\beta_{14_i}(\alpha) - \beta_{14_i}^{data})^2}{\sigma^2_{data_i} + \sigma^2_{MC_i}}, \tag{3.3}$$

where i = ^{16}N, Prompt, Delayed; σ^2_{data} and σ^2_{fit} are errors of β_{14} data and MC respectively. We obtain $\alpha = 0.556 \pm 0.005$. Figure 3.14 shows the result of the fitting and simulations for the α value we have found.

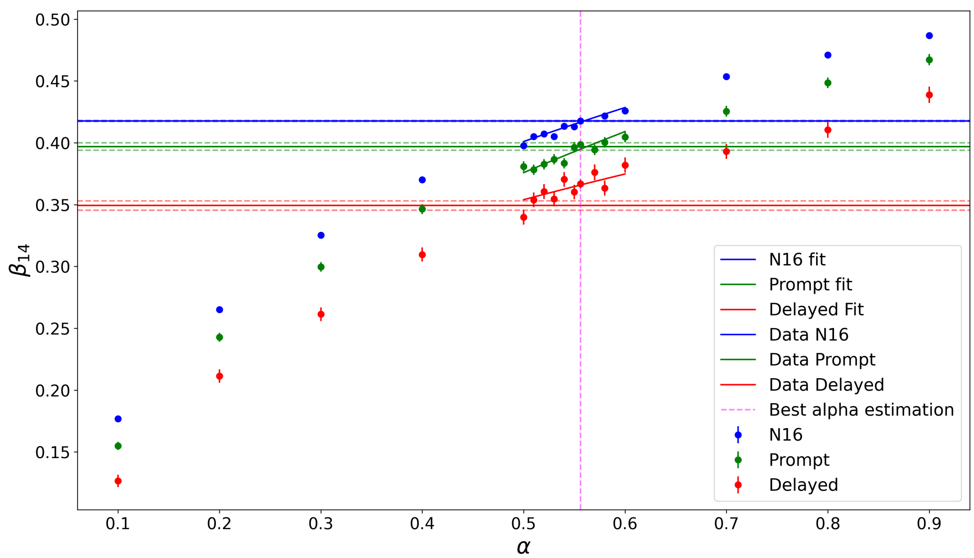

Figure 3.14: The plot demonstrates the simulated β_{14} mean value as the function of the tuning parameter α. Calibration sources with γ - rays of energies 2.2 MeV (Delayed), 4.4 MeV (Prompt), and 6.1 MeV (^{16}N) are used. Optimal value for α is calculated and pictured with the pink dashed line.

3.2.5 Comparison between data and MC

In order to cross-check the correctness of modifications, we also take a look at some quantities, which characterize an event, mentioned in Section 3.1.2.

β_{14} distributions

In the previous section, we were considering only the mean value of β_{14}. To see how good the modification fits the data, we look into the distributions of β_{14}. When we compare β_{14} distribution of ^{16}N default simulation and simulation with sampling to the data, we obtain $\chi^2_{default} = 1085.6/80$ and $\chi^2_{sampling} = 90.4/80$, respectively. For the AmBe source $^{Prompt}\chi^2_{default} = 141.6/80$ and $^{Prompt}\chi^2_{sampling} = 69.6/80$, and $^{Delayed}\chi^2_{default} = 117.6/80$ and $^{Delayed}\chi^2_{sampling} = 78.4/80$ for AmBe Prompt and delayed, respectively. This demonstrates that data is in much better agreement with the modified and tuned MC than with the default one for both ^{16}N and AmBe calibration sources. One can see the distributions of β_{14} on Figure 3.15 and Figure 3.16.

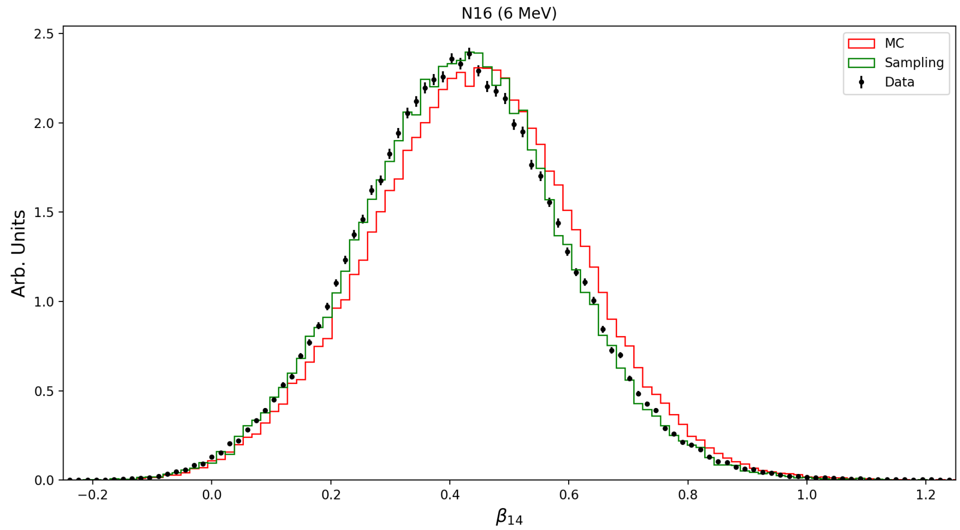

Figure 3.15: Comparison of data, the default MC and modified MC β_{14} distributions of ^{16}N source.

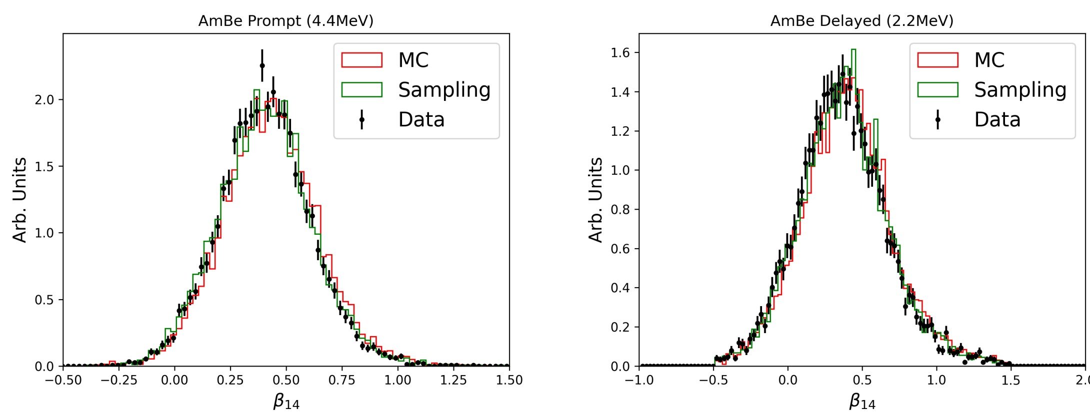

Figure 3.16: Comparison of data, the default MC and modified MC β_{14} distributions of AmBe source prompt (left) and delayed (right) events.

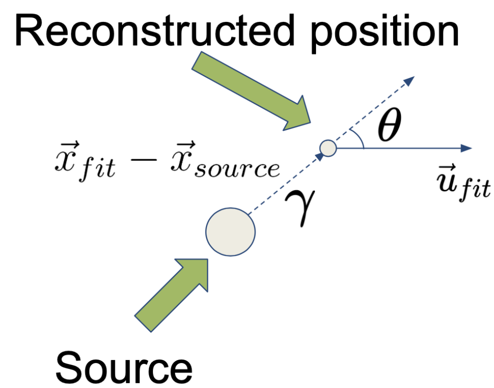

Figure 3.17: A schematics that demonstrates how we obtain θ for direction resolution.

Direction resolution

Compton electrons have high colinearity with the initial direction of the γ-ray that produced them [49]. SNO+ uses this fact for determination of systematic errors of the reconstructed direction $\vec{u}_{fit}$. The reconstructed position of electron $\vec{x}_{fit}$ defines the point where Compton scattering took place. In this assumption, the vector from the source position $\vec{x}_{source}$ to the reconstructed vertex defines the γ - ray direction and a presumable direction of the event. Then, we calculate the angle between the presumable and reconstructed direction $\cos\theta_{dir}$ as:

$$\cos\theta_{dir} = \frac{\vec{x}_{fit} - \vec{x}_{source}}{|\vec{x}_{fit} - \vec{x}_{source}|} \cdot \vec{u}_{fit} \tag{3.4}$$

Figure 3.17 demonstrates mentioned vectors and angles.

We calculate these angles using the default and modified MC with the developed Cherenkov light emission model simulations, as well as using data. ^{16}N source placed in the middle of the SNO+ detector and the selection criteria mentioned in the previous section. Figure 3.18, shows the obtained distribution, where we can see that the sampling model demonstrates better agreement with the data than the default MC. We also calculate χ^2 between the default MC and the data $\chi^2_{default} = 225.34/100$ and between the sampling and the data $\chi^2_{sampling} = 106.37/100$ that confirms our

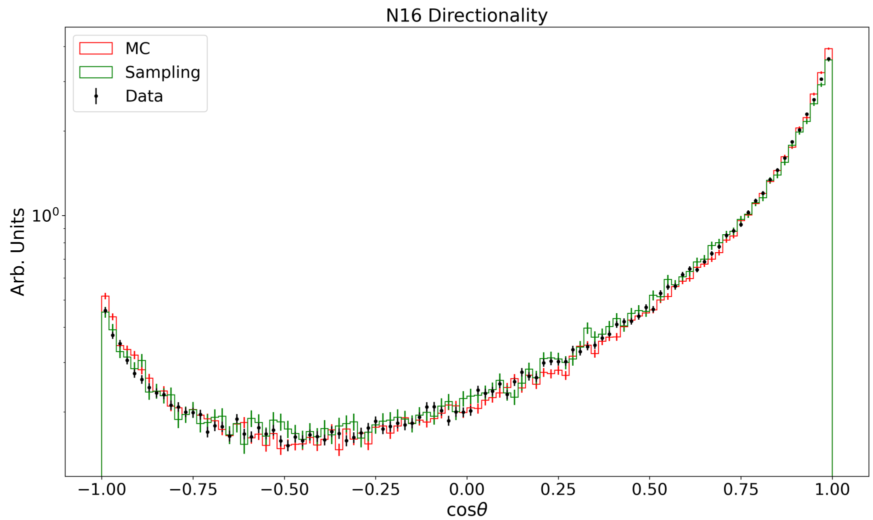

Figure 3.18: A comparison of $\cos\theta_{dir}$ obtained from the default simulation, Cherenkov light sampling model with tuned α and data.

observation.

Cos θ PMT

$\cos\theta_{PMT}$ is the distribution of light within the event in a particle's coordinate system. We obtain it from a dot product:

$$\cos\theta_{PMT} = \vec{u}_{fit} \cdot \frac{\vec{x}_{PMT} - \vec{x}_{fit}}{|\vec{x}_{PMT} - \vec{x}_{fit}|}, \tag{3.5}$$

where $\vec{x}_{PMT}$ is the coordinate of the the triggered PMT. This quantity essentially gives us the information about resulting integrated Cherenkov light distribution, similar to figs. 2.4 and 2.5 or figs. 3.12 and 3.13. However, it also takes into account the SNO+ detector response: geometry, PMTs response, photons transportation. Figure 3.19 shows the $\cos\theta_{PMT}$ distribution for ^{16}N source. The χ^2 value for the default MC $\chi^2_{default} = 8706/200$ when for $\chi^2_{sampling} = 1772/200$. However, fig. 3.20 shows that modification of MC does not make significant impact on the $\cos\theta_{PMT}$ distribution of prompt and delayed AmBe events with the χ^2 value for the prompt events being ${}^{Prompt}\chi^2_{default} = 9312/200$ and ${}^{Prompt}\chi^2_{sampling} = 7523/200$ and for the delayed events

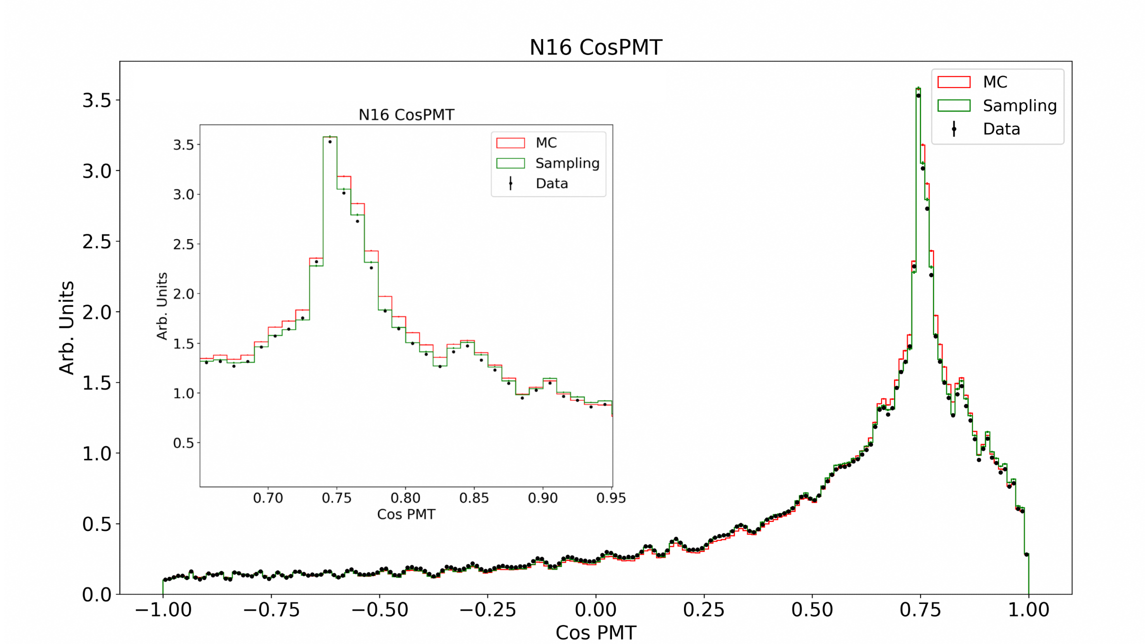

Figure 3.19: A comparison of $\cos\theta_{PMT}$ obtained from the default simulation, Cherenkov light sampling model with tuned α and data for ^{16}N source.

$^{Delayed}\chi^2_{default} = 12374/200$ and $^{Delayed}\chi^2_{sampling} = 10763/200$

Reconstructed position and number of hits

Since we do not change the number of emitted photons, the number of PMT hits will not change. We also do not expect to see any difference in the reconstructed position plots, which relies on the time difference between PMT signals and not spatial distribution of Cherenkov light. Plots on figs. 3.21 to 3.23 demonstrate that the modification does not change data and MC agreement, which agrees with our assumptions.

3.3 Conclusions and potential use in the scintillator phase

In this chapter, we described development of a new Cherenkov light emission method based on the results obtained using the single scattering model for electron propagation. The model is relevant for electrons of energy less than 6 MeV travelling in

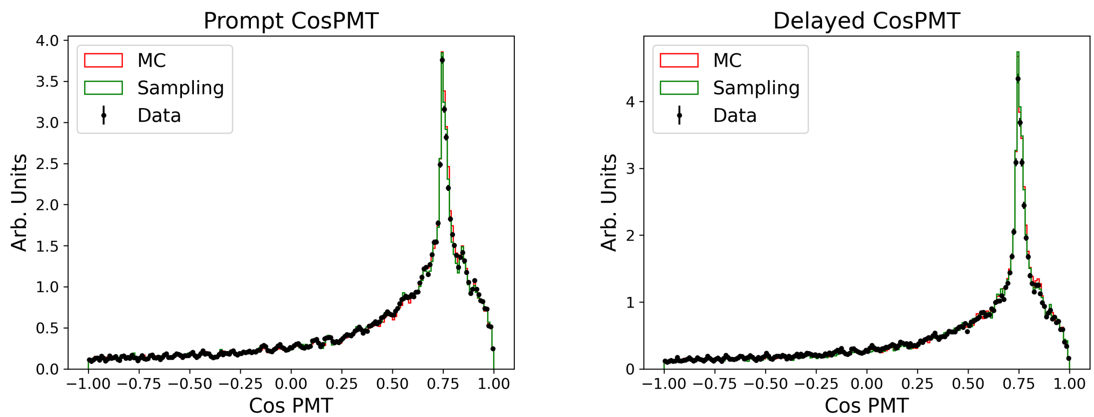

Figure 3.20: A comparison of $\cos\theta_{PMT}$ obtained from the default simulation, Cherenkov light sampling model with tuned α and data for AmBe source prompt (left) and delayed (right) events.

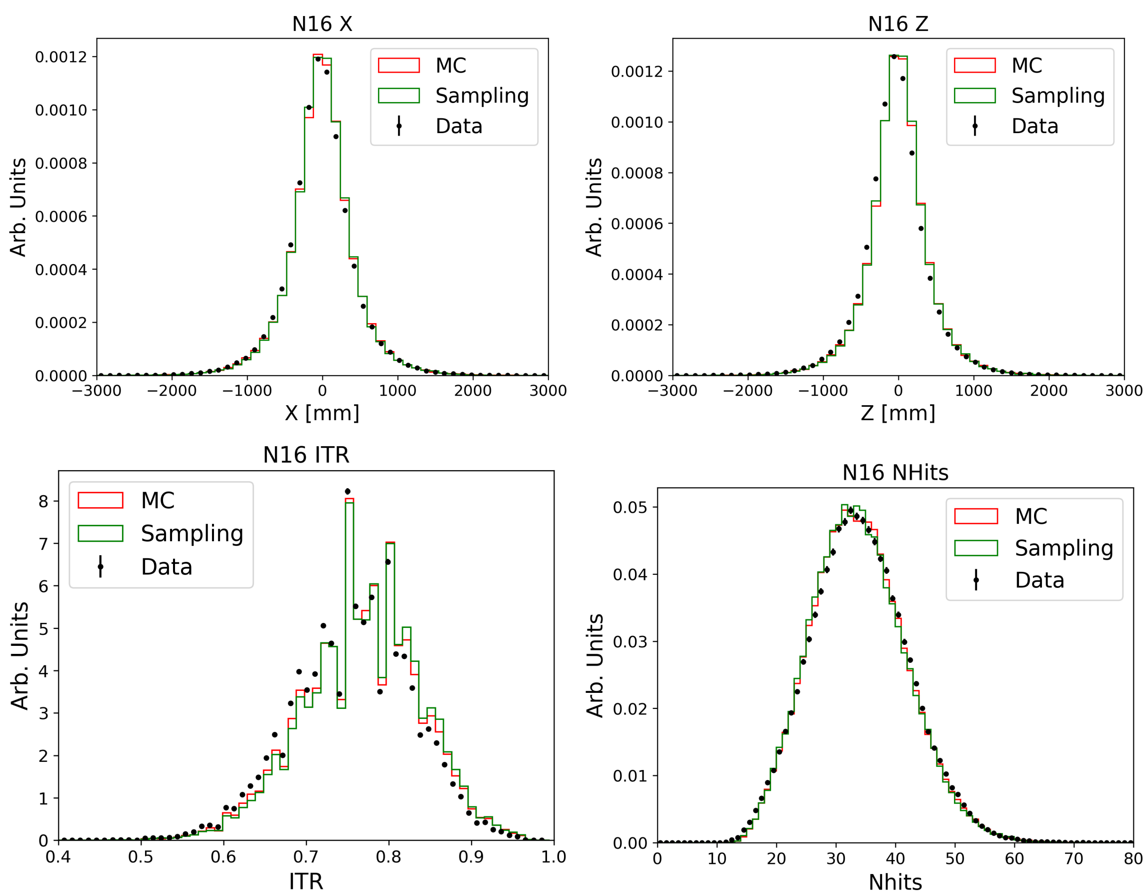

Figure 3.21: Comparison of reconstructed position coordinates, ITR, and number of hits distributions of ^{16}N source obtained from the default simulation, the modified MC and data.

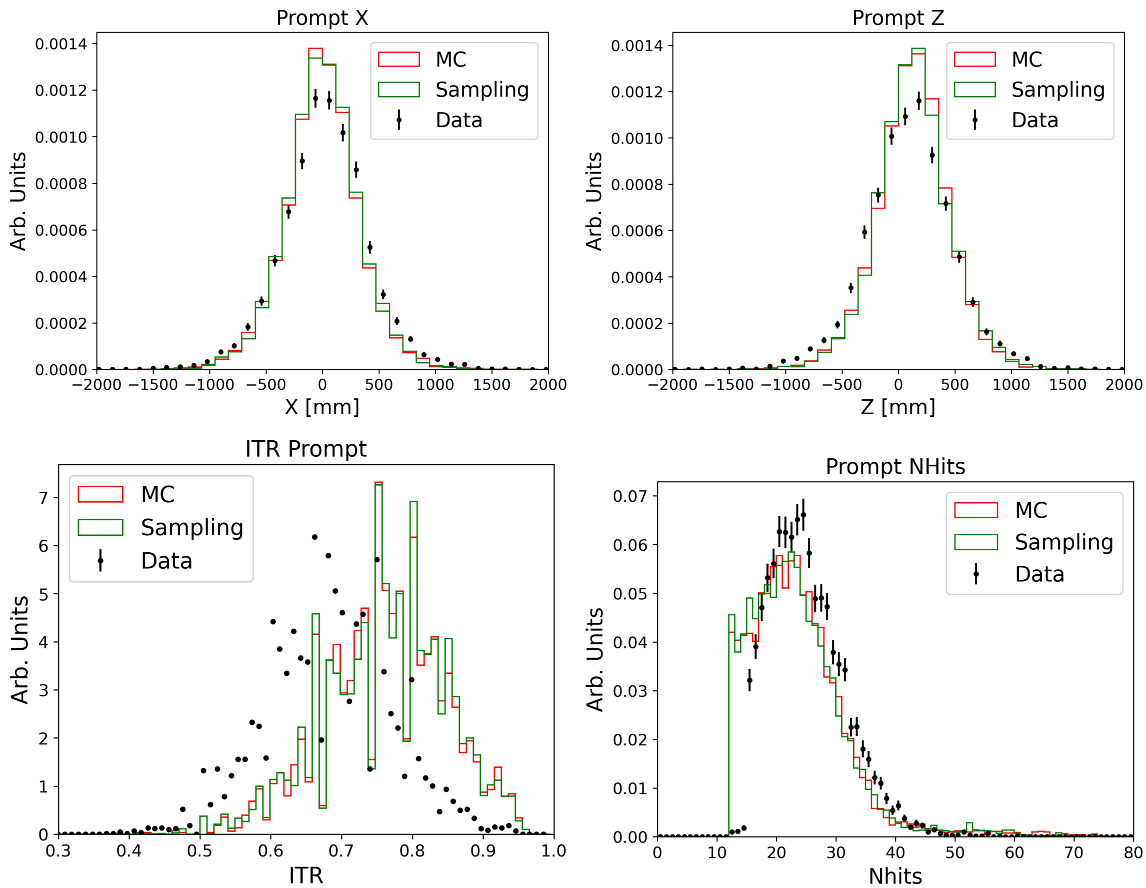

Figure 3.22: Comparison of reconstructed position coordinates, ITR, and number of hits distributions of Prompt events of AmBe source obtained from the default simulation, the modified MC and data.

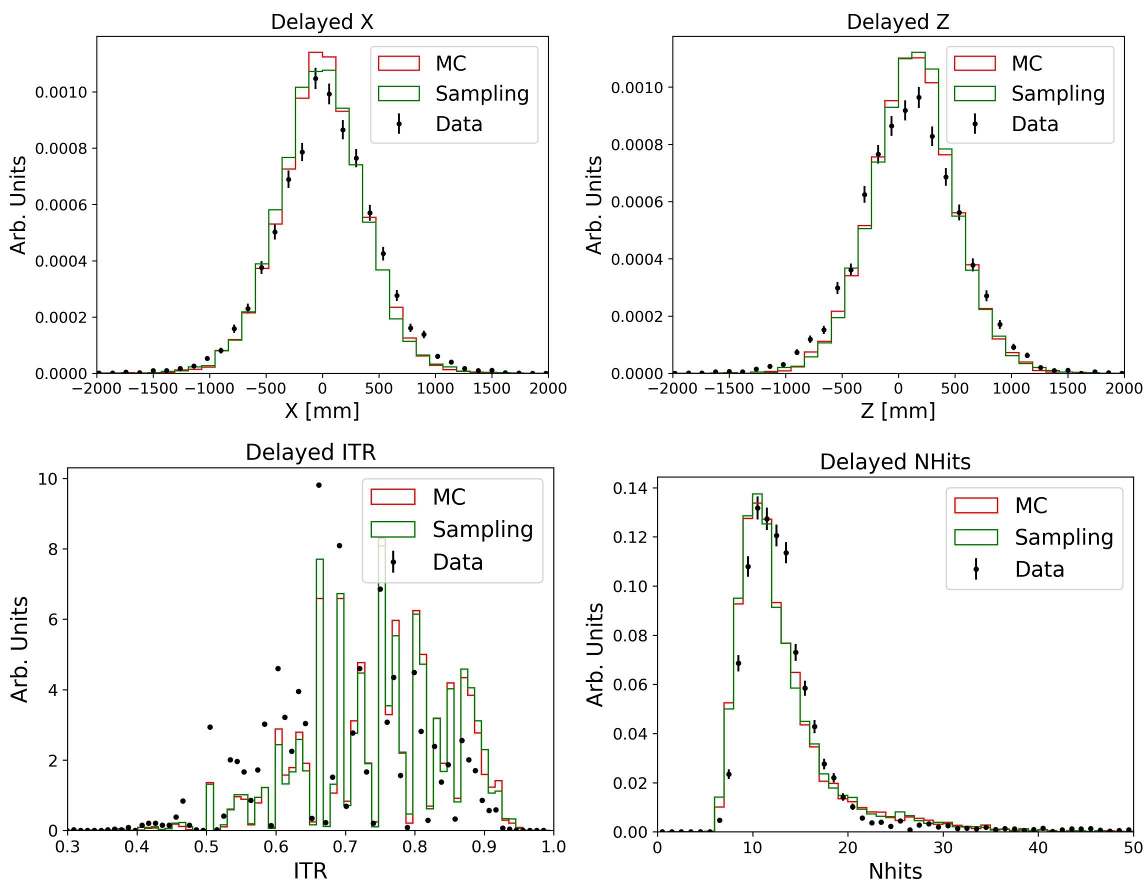

Figure 3.23: Comparison of reconstructed position coordinates, ITR, and number of hits distributions of Delayed events of AmBe source obtained from the default simulation, the modified MC and data.

water, and depends on pre-built tables, which makes it work as fast as the default simulation; reproducing the light emission of exact electron transportation simulation. We implemented the method in the Geant4 package and used SNO+ calibration data to tune the free parameter α. As the result, we were able to match data and MC mean values from Gaussian fit of β_{14} parameter for ^{16}N and AmBe calibration sources with the values specified in table 3.3. We also improved agreement between data and MC of total angular distribution (see fig. 3.19) and directionality plot (see fig. 3.18), while the other variables remained unaffected in comparison to the default MC. The fix of the β_{14} discrepancy, which is used in water analysis for separation of different types of events, as well as improvement of direction resolution (see fig. 3.18), may decrease total systematic error. For example, in nucleon decay analysis [50], β_{14} has a contribution of 3% to 10% to the count rate systematic uncertainty, depending on the decay mode. The other major contribution to the systematic error in this analysis is direction systematic that contributes from 10% to 30%. So, we can expect total improvement of the systematic error by 15% to 40%.

The proposed method may also be used in the scintillator phase if usage of Cherenkov light for event reconstruction will be justified. Instead of water, the electron will be travelling in a new material – scintillator. Therefore, one has to build new tables and tune the parameter of the model again, following the steps described in the current chapter.

Calibration source	^{16}N	AmBe Prompt	AmBe Delayed
Data β_{14}	0.4176 ± 0.0004	0.3969 ± 0.0026	0.3497 ± 0.0038
Default MC β_{14}	0.4414 ± 0.0005	0.4224 ± 0.0022	0.3866 ± 0.0032
Sampling β_{14}	0.4177 ± 0.0007	0.3986 ± 0.0025	0.3669 ± 0.0035
Data σ	0.1727 ± 0.0003	0.2008 ± 0.0020	0.2899 ± 0.0032
Default MC σ	0.176 ± 0.0003	0.2089 ± 0.0017	0.2967 ± 0.0027
Sampling MC σ	0.1714 ± 0.0005	0.2067 ± 0.0018	0.2923 ± 0.0030

Table 3.3: β_{14} mean values and σ from a Gaussian fit comparison.

Chapter 4

Optical crosstalk in SiPMs as a challenge for Cherenkov light detection

Photodetectors are devices whose purpose is to convert light or electromagnetic radiation into a measurable signal like current or voltage [51]. They are commonly used in particle physics detectors exploiting Cherenkov and scintillator light. Development of photodetectors made possible pattern recognition of Cherenkov rings created by low energy electrons, which lead to the creation of large water-filled neutrino detectors, including SNO+. However, new generation experiments require improvement of the light detecting systems. For example, SNO+ would be able to make use of Cherenkov light even in the scintillator phase if the PMTs had a better time resolution [52, 53]. One way of addressing this problem is to consider using SiPMs or hybrid photodetectors [54]. In this chapter, we give an introduction to the operational principles of silicon photomultipliers (SiPMs) and the challenges of using them. We describe the phenomenon of optical crosstalk and develop a way of predicting it by means of a Monte-Carlo simulation. To verify the simulation, we use the optical crosstalk measurements of HPK VUV4 and FBK HD3 SiPMs [55].

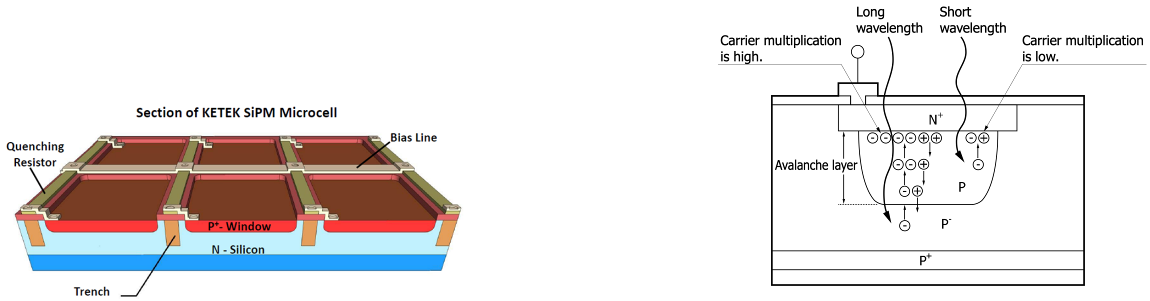

Figure 4.1: Left figure [56] shows a SiPM schematics, which consists of SPADs separated by trenches and electronics. Right figure [57] shows schematics of a SiPM cell, illustrating long and short wavelength photons detection.

4.1 SiPM

4.1.1 What is a SiPM

Silicon photomultipliers (SiPMs) are photodetectors of low intensity light down to a single photon. They consist of arrays of single-photon avalanche diode (SPAD) cells (see fig. 4.1 (left)) separated by trenches and readout electronics. SPADs are designed specifically for single photon detection. They generate current or voltage with internal photoeffect when the thick, weakly doped depleted region is irradiated by light and as the result charge carriers (electrons or holes) are created. Reverse biased voltage is applied to photodiode, and normally the gain of a semiconductor photodetector is linearly proportional to the biased voltage. However, when the voltage passes a critical value, called breakdown voltage, the detector starts generating a self-sustaining cascade of secondary charge carriers. SiPMs are operating this regime, called Geiger mode. As one can see on fig. 4.1 (right), because of the potential difference, charge carriers drift towards a highly doped metallurgical junction region. When crossing this region, they create an avalanche that generates thousands of new charge carriers and gives a gain of $10^5 - 10^6$ [7]. In this regime, the detector can only specify that one or more photons were detected, but cannot count them. The avalanche is a self-sustaining process – without a quenching the current flow would be constant. So, the discharged created by the avalanche is quenched by a quenching resistor located in every pixel

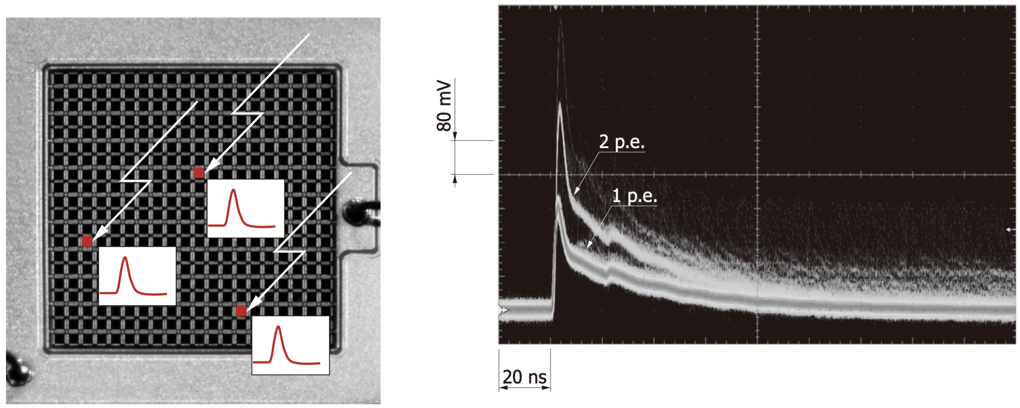

Figure 4.2: Left figure illustrates how a SiPM does photon counting. Right figure demonstrates the signal one obtains from a SiPM. One photoelectron (p.e.) peak corresponds to 1 photon detection. If 2 photons were detected the signal sums up and results in a higher 2 p.e. peak. Both images were taken from [57].

(see fig. 4.1). The current created by the discharge makes the operating voltage drop below the breakdown voltage and SiPM enters the recovery phase. After typically $\leq$ 100ns [7] it's over the breakdown voltage again and ready to detect new photons. The discharge and recharge from each activated SPADs create a waveform that is depicted on fig. 4.2. The height of the 1 p.e. waveform corresponds to one count in a SiPM. SiPMs make use of this binary operational mode of cells and sum up the waveform, forming the final output signal as one can see on fig. 4.2 (right). Cells have typical dimensions of 15-70μm [58] and the size of the SiPM active area varies from 1.3 mm $\times$ 1.3 mm to 6 mm $\times$ 6 mm [59], so a typical SiPM consists of thousands of SPADs.

4.1.2 Optical crosstalk (OCT)

SiPMs are robust and low cost detectors, however, they suffer from an unwanted process of optical crosstalk. When the amplification process happens, due to the high acceleration in the electric field, thousands of secondary charge carriers may emit photons, known as secondary photons. These photons may be absorbed within the cell or a trench, be emitted out of the SiPM surface or travel through the SiPM to

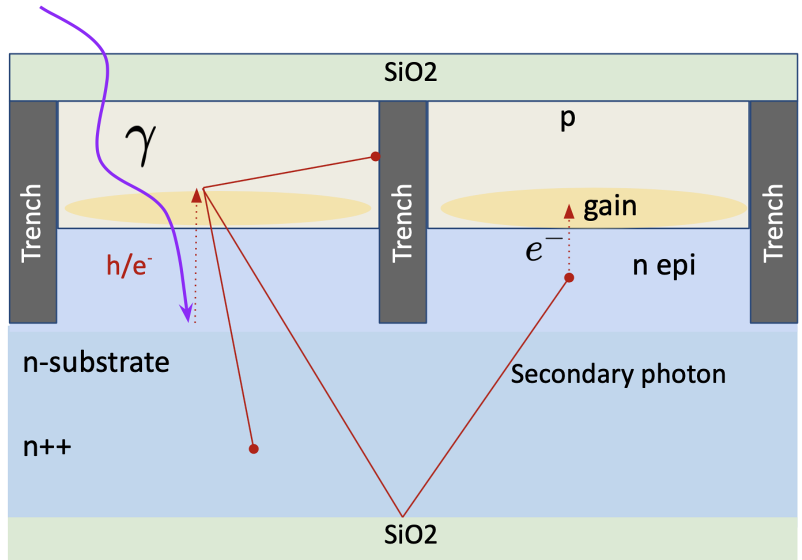

Figure 4.3: Illustration of the optical crosstalk mechanism in SiPM. A photon (violet) creates an avalanche that emits secondary photons (red lines). The secondary photons can be absorbed in the silicon bulk, in a trench or in another cell, creating a secondary avalanche.

another cell and trigger it (See Fig. 4.3). This causes an additional signal that can be misinterpreted as the detection of more photons.

This process sets the limits on the density of SiPMs cells so prediction of the optical crosstalk rates is an important task for designing new models of SiPMs. Further details on optical crosstalk one can find, for example, in [60].

4.1.3 Prediction of the optical crosstalk

The appearance of the optical crosstalk process is unavoidable, however, we can characterize and minimize this effect. It is possible to measure OCT in the lab [55, 61], but this is possible only after the construction of a detector. For the development of a new model of SiPM, we would like to know OCT levels a priori to optimize the geometry and minimize the effect. To predict possible levels of OCT, some analytical models (see Sec.2 of [62]) and calculations [63, 64] were done. We complement them and create a tool by using a Monte-Carlo simulation.

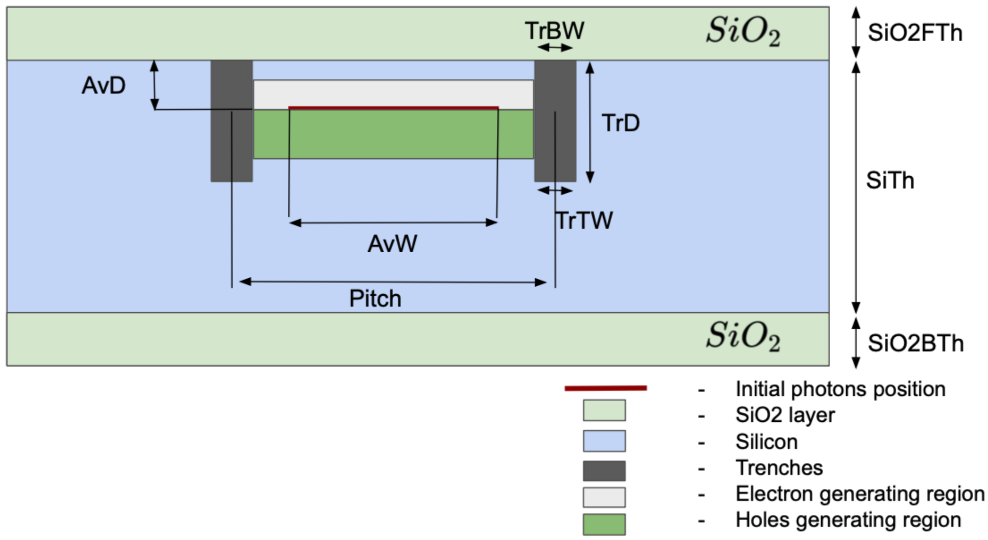

Figure 4.4: Dimension variables from table 4.1 .

4.2 Simulation

This work was started in TRIUMF [65] and gave the first estimates of the OCT in HPK VUV4 and FBK HD3 SiPMs. The simulation process includes creation of photons in the avalanche region, and its propagation and tracking inside of a SiPM with a defined geometry. We take this code as the starting point, eliminate errors, modify it, and develop a different analysis technique. For the simulation verification we also use HPK VUV4 and FBK HD3 SiPMs, whose characteristics were measured by our collaborators in TRIUMF [55]. We use Monte-Carlo simulations with the Geant4 package [22], therefore, we need to set up geometry, materials and its properties, give a particle list, and processes that the defined particles will be involved.

4.2.1 Geometry and simulation process

The geometry of the SiPM can be described with a square grid $N_{cell} \times N_{cell}$ identical cells that represent SPADs. The schematics of a cell can be found on fig. 4.4. The main bulk of the detector is silicon, and the boundaries of the silicon at the top and bottom of the detector are thin silicon oxide layers. Trenches can be made from different materials and they can be changed, but we consider only tungsten (for HPK VUV4) and polysilicon (for FBK HD3). The space around the SiPM is filled with air. The variables specified on the schematics are different for every specific SiPM model and can be effortlessly changed in the code. The dimensions used for the simulation of HPK VUV4 and FBK HD3 are given in table 4.3. We also divide each SPAD to $N_{bin} \times N_{bin}$ bins, so a geometrical grid appears as shown on fig. 4.5. We inject the photons at the AvD in each bin separately and then they are propagated within the SiPM until they are either absorbed or leave the simulation region. In any case, we record their initial position, initial momentum, wavelength, final step position (absorption point), second last step position (the track point right before absorption happened) to be able to reconstruct the direction of the last step.

The code of the simulation and analysis scripts are uploaded to GitHub [66, 67]. Prerequisites and short instructions for running the code are given in the README.md file.

4.2.2 Physics involved

Scintillation

To mimic the avalanche region, which we assume emits secondary photons isotropically, we add scintillator properties to the silicon bulk and inject low energy (several eV) electrons in the avalanche region to create light. Each electron produces about 1000 scintillation photons before getting absorbed in silicon within ∼nm depth. The refractive index and mean free path of photons depend on its wavelength. Therefore, we need to set up the scintillation emission spectrum of secondary avalanches. So far, we used a uniform distribution, but it can be changed to a user defined one.

Absorption and Boundary scattering

Absorption kills photons depending on the absorption length of a material. Boundary scattering is an important part of the current simulation and a possible direction to explore in order to improve accuracy. Currently we assume that a photon's transition between SiPM regions happens through perfectly smooth surfaces of dielectric materials [68]. To calculate these, we need to know refractive index (RI or n) and extinction coefficient k of the materials. RI and k for silicon and polysilicon were taken from [69] p.113-118 and [70]. Polysilicon RI and k can be anywhere between crystalline silicon (c-Si) and amorphous silicon (a-Si) depending on the polysilicon crystal structure disorder. Therefore, the true values of coefficients for poly-Si will depend on the fabrication process. Information regarding Tungsten properties was taken from [71]. For the air, we use refractive index RI = 1 and absorption length of 1m.

Optical processes that are assumed to have negligible contribution

1. Rayleigh scattering - interaction length is metres for the used materials and specified wavelengths region, so it is not relevant for mm scale geometry.

2. Mie scattering takes place when the scattering media consists of particles that are compatible in size to the incident photons wavelength. Atoms of silicon are much smaller than hundreds of nm photons we are interested in, so the process is irrelevant for our studies.

4.3 Analysis (Simulation verification)

To understand and verify the simulation, we compare it to the measured performance of real SiPM models. The verification steps are shown on fig. 4.6. From the parameters listed on fig. 4.4 and in table 4.1 there are only few that are provided by the manufacturer. The others were measured and have some tolerance. We also cannot be sure that we precisely know the properties of the materials, as was mentioned

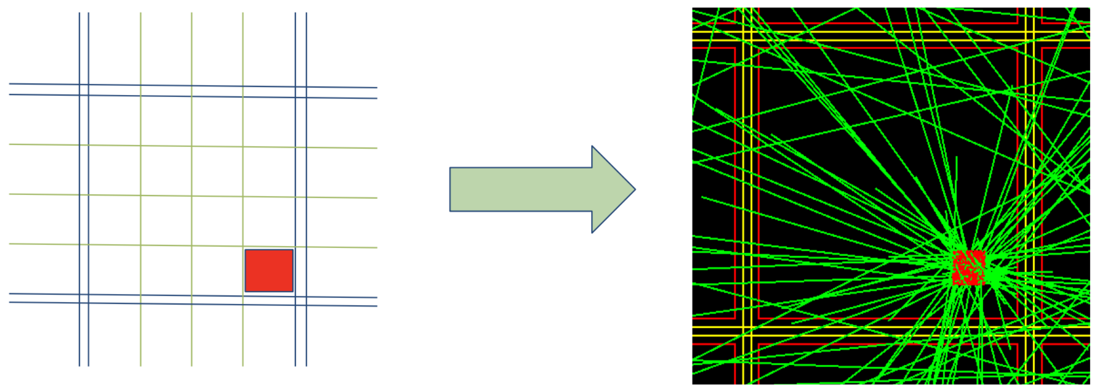

Figure 4.5: To inject light we divide a cell of the SiPM into $N_{bin} \times N_{bin}$ bins. Schematics on the left and a render from Geant4 on the right.

Item	Variable Name	Manufacturer information
Pitch width	Pitch	Yes
Silicon thickness	SiTh	Yes
Silicon dioxide front thickness	SiO2Fth	Yes
Silicon dioxide back thickness	SiO2Bth	Yes
Trench base width	TrBW	No
Trench top width	TrTW	No
Trench depth	TrD	No
Avalanche region depth	AvD	No
Avalanche region thickness	AvTh	No
Avalanche region width	AvW	No
Number of cells	CellNum	Yes
Emission spectrum	User-defined	No
Refractive indices	–	No
Trench material	Poly Si or W	Yes

Table 4.1: List of geometry variables used in the simulation and if they are provided by the manufacturer.

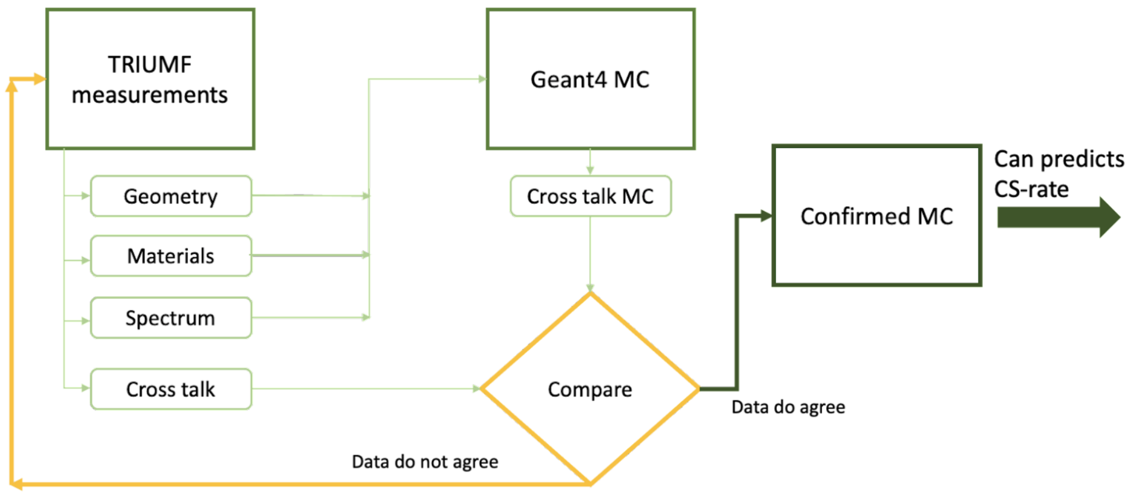

Figure 4.6: The simulation verification steps diagram.

	TrBW	TrTW	TrD	AvD	AvW
HPK VUV4	0.1 - 1 μm	0.1 - 1 μm	1 - 5 μm	0.8 $\pm$ 0.2 μm	0.7-0.9 $\cdot$ Pitch
FBK HD3	0.1 - 1 μm	0.1 - 1 μm	1 - 5 μm	0.145 $\pm$ 0.01 μm	0.7-0.9 $\cdot$ Pitch

Table 4.2: Limits on the SiPM dimensions that are not provided by a manufacturer.

in Section 4.2.2. Therefore, we put the geometry and materials information that we know (such as dimensions of the SiPM, size of the pitch) to the simulation unchanged, and at the same time we have several parameters that we can vary in the limits we consider reasonable for the tested models (see table 4.2), including the fact that the avalanche region thickness is close to zero. The simulation gives an estimation of crosstalk level so we can find the geometry parameters combinations that match the estimated crosstalk level with the measured OCT. Since there are many variables that are not provided by a manufacturer we may find more than one combination of the parameters that give the correct answer.

4.3.1 Calculation of the optical crosstalk probability

The avalanche in the active region can be caused both by electrons and holes. However, the probability $P_h(z)$ of creating a holes-driven avalanche and probability $P_e(z)$ of creating an electrons-driven avalanche are the functions of the distance from the surface of a SiPM. Therefore, the probability of creating an avalanche is given by [72]

$$P_{av}(z) = P_h(z) + P_e(z) - P_h(z)P_e(z), \tag{4.1}$$

where $P_h(z)$ and $P_e(z)$ are the probabilities of initiating a chain reaction of ionization (avalanche) by holes and electrons respectively. Crosstalk is the probability of creating a secondary avalanche in a nearby cell. The formula is then

$$P_{av_{sec}}(z) = P_{h_{sec}}(z) + P_{e_{sec}}(z) - P_{h_{sec}}(z)P_{e_{sec}}(z), \tag{4.2}$$

where $P_{h_{sec}}(z)$ and $P_{e_{sec}}(z)$ are the probabilities of initiating a secondary avalanche by holes or electrons respectively.

According to [73], we can simplify the model by dividing active region into two parts that do not intersect, considering effective depth parameters. The division into electron and holes avalanche generating regions is illustrated on fig. 4.4. The avalanche creating probability is constant within each of these effective regions and zero outside of it. The probability $P_{hh}(z)$ of secondary photon hitting holes-driven avalanche region or probability $P_{eh}(z)$ of secondary photon hitting electrons-driven avalanche region are defined by the number of photons absorbed in each of the effective regions. Therefore, the probability for a photon to cause a secondary hole driven avalanche is

$$P_{h_{sec}}(z) = P_h(z)P_{hh}(z) = P_h(z)\frac{N_{ph_h}}{N_{ph_{tot}}}, \tag{4.3}$$

where N_{ph_h} is the number of secondary photons that ended up in the holes-driven avalanche region – $N_{ph_{tot}}$ is the total number of photons. By analogy, the probability for a photon to cause a secondary electron driven avalanche is

$$P_{e_{sec}}(z) = P_e(z)P_{eh}(z) = P_e(z)\frac{N_{ph_e}}{N_{ph_{tot}}}, \tag{4.4}$$

where $P_{eh}(z)$ is the probability of secondary photon hitting electrons-driven avalanche region, N_{ph_e} is the number of secondary photons that ended up in the electrons-driven avalanche region. The average number of photons emitted in each avalanche N_{ph} is the function of over voltage and can be calculated as

$$N_{ph} = G(V)\gamma_y, \tag{4.5}$$

where $G(V)$ is gain of the SiPM and γ_y is the light yield of one charge carrier in avalanche. Considering this, the probability of an avalanche induced by one or more photons is:

$$P_{avfull}(\geq 1\gamma) = 1 - (1 - P_{av_{sec}})^{N_{ph}} \tag{4.6}$$

To manipulate data efficiently, we divide the x-y plane of a SPAD into N_{bin}^2 bins of the same size. For each bin, we calculate $P_{h_{sec}}$ and $P_{e_{sec}}$. Using the eq. (4.6), we can calculate the probability of an avalanche being induced in a specific bin $P_{avfull_{bin}}(\geq 1\gamma)$. If $P_{avfull_{bin}}(\geq 1\gamma) \ll 1$, meaning the bin size is small, we can neglect the probability of several photons hitting the same bin and also calculate the avalanche probability in a cell as a direct sum of probabilities for the bins because the cross-terms $P_{avfull_{bin},i}(\geq 1\gamma) \cdot P_{avfull_{bin},j}(\geq 1\gamma)$ will be negligible. Then

$$P_{av_{cell}}(\geq 1\gamma) \simeq \sum_{i}^{N_{bin}} P_{av_{bin},i}(\geq 1\gamma) \tag{4.7}$$

To get the full cross talk probability with at least one avalanche, neglecting second order P_iP_j terms, we are summing up the probabilities for the cross talk in each cell – neglecting a possibility that several photons could hit the same cell during a one photodetection:

$$P_{CT} = \sum_{i}^{N_{cell}} P_{av_{cell},i}(\geq 1\gamma) \tag{4.8}$$

The effective depth parameters, P_e and P_h are taken from [73].

4.3.2 Acquiring light emitted from the SiPM

Another way to use simulation is to estimate the amount of light emitted from the surface of the SiPM as the consequence of OCTs. As shown on fig. 4.7, we assume that secondary photons are emitted isotropically and some of them are able to leave

Item	Hamamatsu VUV4 [μm]	FBK HD3 [μm]
Pitch width	50	35
Silicon thickness	300	300
Silicon dioxide front thickness	1	1
Silicon dioxide back thickness	1	1
Trench base width	1	1
Trench top width	1	1
Trench depth	5	3
Avalanche region depth	1	0.1
Avalanche region thickness	0.01	0.01
Avalanche region width	40	32
Number of cells	25	25
Emission spectrum	Uniform	Uniform
Trench material	Tungsten	Polysilicon

Table 4.3: Dimensions used in the simulation of the FBK HD3 and Hamamatsu VUV4 SiPMs that corresponds to the results demonstrated on fig. 4.9. Taken from [65]. Some guesses were made for the parameters listed in table 4.2.

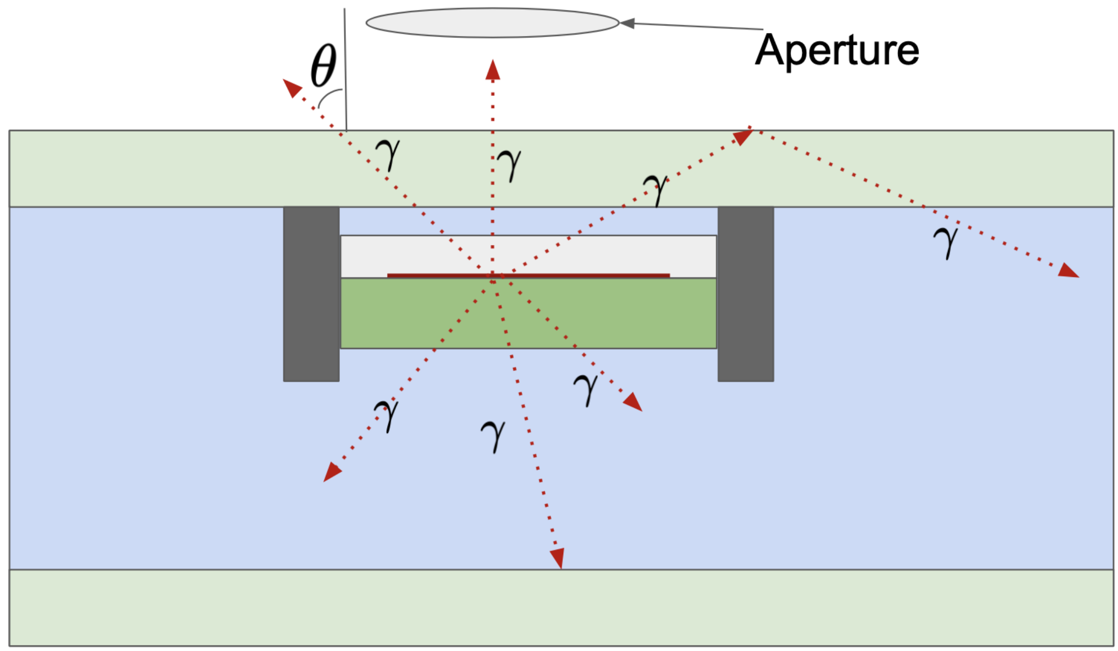

Figure 4.7: The light produced within the avalanche region (red dotted lines) leaves the SiPM and hits the aperture of a measuring device.

the SiPM. In order to build an image of the light emitted from the SiPM, we record the direction of photons leaving the photodetector and then select those with an angle to a normal vector of the SiPM surface equal or less to $\theta_{aperture}$, which corresponds to the aperture acceptance angle of a device that records the photons.

First, we inject light that corresponds to an initial avalanche and calculate OCT levels for each bin, as described in Section 4.3.1. As for the result, we obtain a map that describes the probability of absorbing a photon and creating a secondary avalanche. It is schematically pictured on fig. 4.8 (middle), which is essentially a binned probability density function (PDF) of having a secondary avalanche as the function of X and Y coordinates. A real SiPM consists of hundreds and thousands of cells but we simulate only the few closest to the initial one and consider our SiPM endless in X and Y coordinates so the boundary effects can be neglected. Therefore, we can reuse the initial cell data. We shift it to the corresponding bins of other cells by assigning the weights obtained from the photon's absorption map. Schematics of this process can be

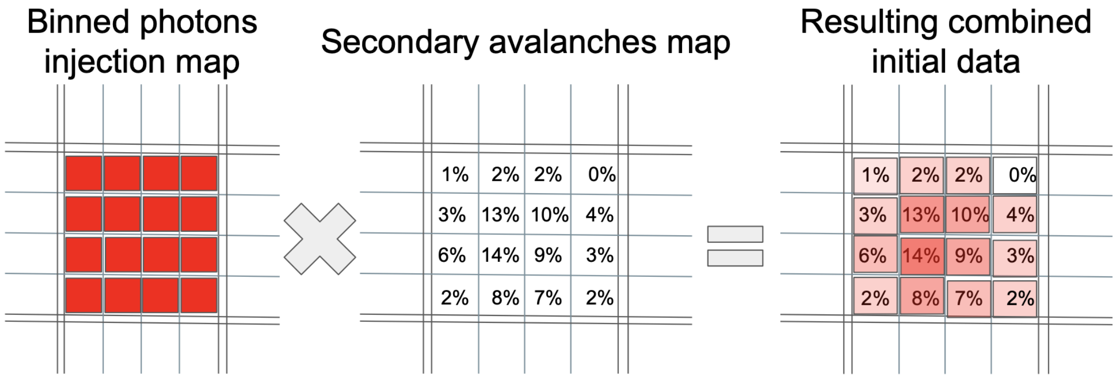

Figure 4.8: Schematics description of bins and reusing the initial cell data. The double lines depict trenches and single lines show bins boundaries. On the left we have uniformly distributed initial data. The avalanches probabilities map in the middle specifies a fraction of data we take from the initial bins cells. By just recombining the initial cell data we obtain the photons distribution as if we simulated avalanches in this cell. The probabilities illustrated on the schematics are arbitrary and are not taken from data.

found on fig. 4.8. The light from the secondary avalanches may also induce OCT. We can take this into account by getting the last positions of the photons created in the secondary avalanches and following steps of Section 4.3.1 and in this subsection above. If needed, it can be repeated for tertiary and higher order avalanches. In the obtained data set, we select the photons that hit the aperture, as depicted on fig. 4.7, and then put the positions of them escaping the surface of the SiPM into a 2D histogram.

4.3.3 Comparison to the data

In order to proceed through the verification steps, as described in the previous section, we use FBK HD3 and Hamamatsu VUV4 SiPMs as a reference. With the dimensions specified in table 4.3, we run the simulation and go through the analysis steps described in Section 4.3.1 and Section 4.3.2. As was mentioned in Section 4.3.1, the resulting $P_{CT} = P_{CT}(V)$ is the function of voltage, so we are able to build a plot of optical crosstalk vs voltage using eq. (4.6), $G(V)$ from [73, 74], and γ_y from [55]. Figure 4.9 shows the simulated OCT levels in comparison to the measured [55]. We can see that

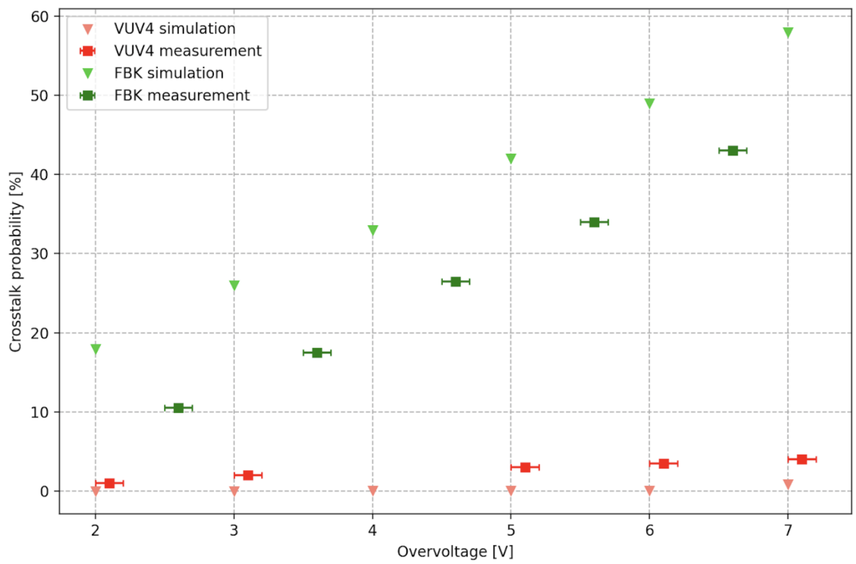

Figure 4.9: FBK HD3 and Hamamatsu VUV4 SiPMs measured (adapted from [55]) and simulated probabilities of OCT as the functions of over voltage. The error bars for the probabilities are present but small and smaller than the marker size.

by using the parameters from table 4.3, the simulated crosstalk for the FBK SiPM is higher than the measured one – but the Hamamatsu SiPM simulation underestimates the OCT level. Therefore, further fine calibration, as shown on fig. 4.6, may be able to help achieve the agreement.

We explored how changing the trench depth and width influences the crosstalk in Hamamatsu SiPM with the results presented on fig. 4.10. One can see that there is a strong dependence of OCT on trenches depth. If we fix a trenches width parameter (fig. 4.10(right)), and choose a value for trenches depth between 1 μm and 2 μm, we will be able to fit it to the experimental OCT level of about 3.7% measured at 7V overvoltage.

For building a picture of the light emitted from the SiPM surface, as described in Section 4.3.2, we conduct a simulation with the same parameters listed in table 4.3 at 7V overvoltage. We use $\theta_{aperture} = \arcsin 0.45$ and take into account two orders of OCT. As the result, we obtain images that are shown on fig. 4.11. Qualitatively, simulated light emission for FBK is in a good agreement with the measured data. Due

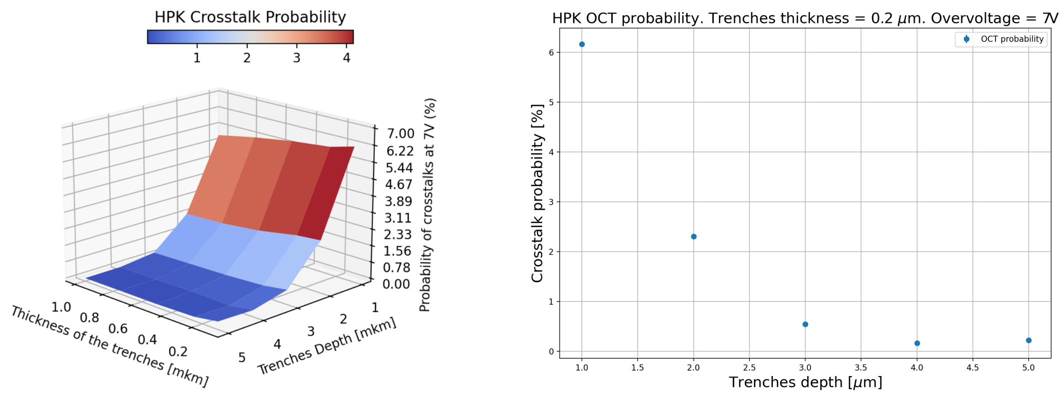

Figure 4.10: Hamamtsu VUV4 (HPK) optical cross talk with 7V overvoltage as the function of trenches depth and width (left) and OCT as the function of trenches depth with trench width fixed at 0.2 μm (right).

to the high OCT levels in the FBK SiPM, taking into account second order cross talk significantly changes the picture (see fig. 4.12), which means that a cross structure one can see on fig. 4.11(top) for the FBK is probably caused by second and higher orders of OCT. For the Hamamatsu detector, we see artifacts that appear because we change the trench material from poly silicon to tungsten. It may be caused by incorrect material properties, but so far we were not able to address this issue.

4.4 Conclusions and future work

In this chapter we described the development of a simulation tool for estimation of optical cross talk levels in SiPMs. The code outputs the OCT levels but is also capable of measuring the light emitted from the surface of the photodetector. We compared, measured, and simulated OCT levels for FBK HD3 and Hamamatsu VUV4 SiPMs. They do not match for the default parameters from table 4.3, but as a proof of concept, it was demonstrated with the Hamamatsu detector that the agreement can be achieved by varying trenches depth and width (see fig. 4.10). More examples of varying parameters can be found in appendix A. However, the full analysis should include studies of how all the parameters that we do not know precisely (see table 4.1)

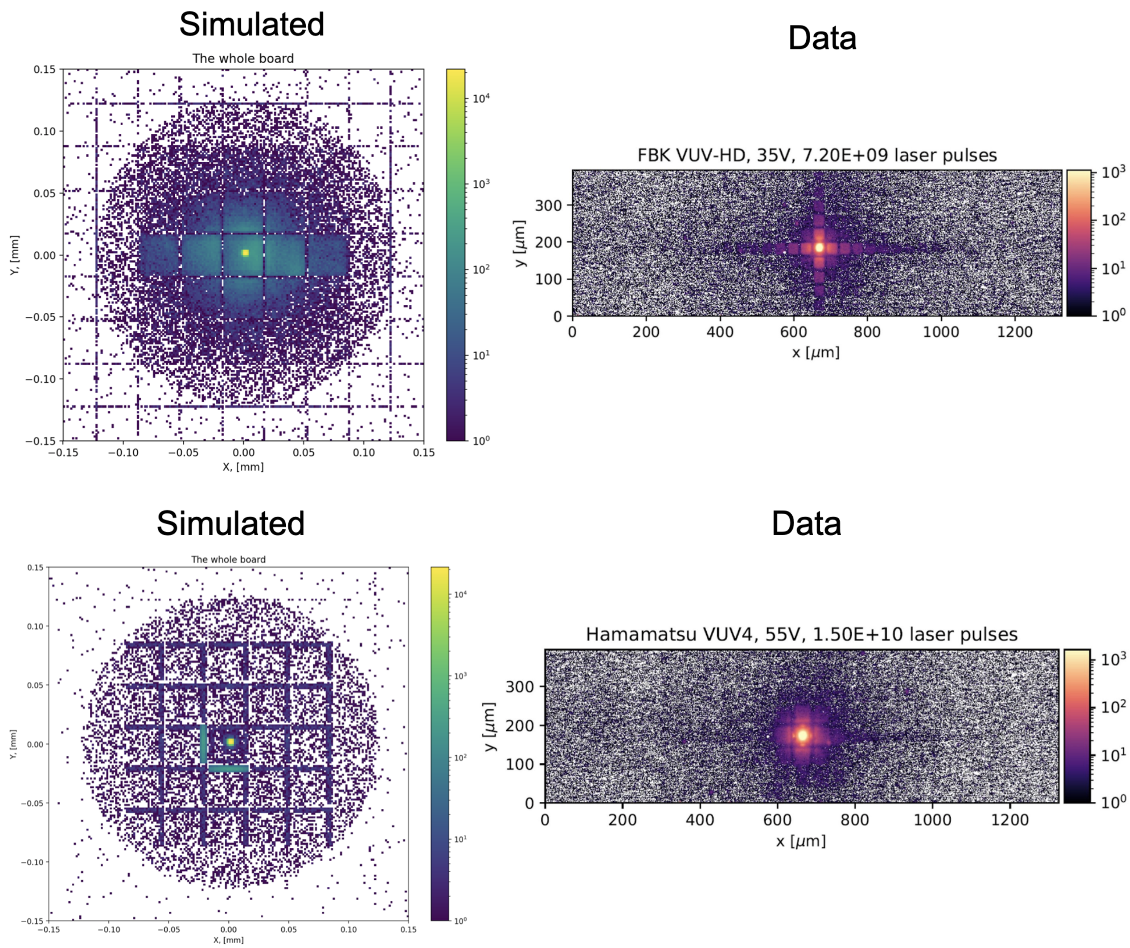

Figure 4.11: Comparison between simulated (5 x 5 cells) and measured (adapted from [75]) light emitted from the SiPM surface. Top corresponds to FBK and bottom to Hamamatsu detectors. For Hamamatsu SiPM we see artifacts that were caused by changing trenches materials from poly silicon to tungsten. The circular pattern one can see on the simulated images is probably caused by a strict restriction on the emitted light acceptance to reproduce the aperture width of a measuring device (see fig. 4.7).

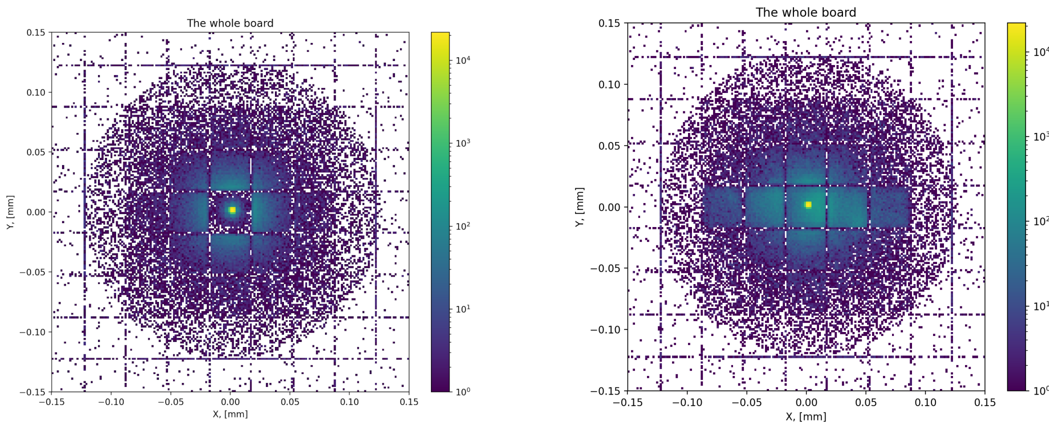

Figure 4.12: Simulated light emitted from the surface of FBK with one (left) and two (right) orders of OCT taken into account.

influence the OCT for both SiPM models.

To decrease uncertainty, we can also reconstruct the emission spectrum by the means of simulation. We have spectra of the light leaving a SiPM [55] and we also can get the spectra of the light emitted from the SiPM from the simulation. To match simulated spectrum to the measured one, we assign a weight to each wavelength bin. We apply the weights to the known initial distribution of injected light (uniform) and can obtain the true emission spectra of avalanches in SiPMs.

We built images of emitted light from FBK HD3 and Hamamatsu VUV4 SiPMs (see fig. 4.11). The FBK HD3 simulation repeats the cross structure of the emitted light we see in the data – which can be explained by secondary and higher levels of OCT (see fig. 4.12). Another reason for that is polysilicon trenches that may serve as wave guides and let the light travel further into other cells. This can be checked with the simulation code by tracking the secondary photons to see if they had multiple reflections within trenches. The Hamamatsu VUV4 image does not correspond to the data and why changing trenches material to tungsten disturbs the image of emitted light has to be understood.

Chapter 5

Conclusions

In the first part of this thesis, we studied the mechanism of Cherenkov light emission and concluded that scattering of electrons of the MeV energies in water does not influence the coherence of the radiation, down to electrons of 0.3 MeV energy, which are near the threshold for Cherenkov light production, and are below the detection threshold for SNO+ (water phase). However, we found out that the choice of the scattering model for propagation of electron in Geant4 significantly changes the total Cherenkov light angular distribution. We developed a new Geant4 Cherenkov light radiation model that corresponds to the light emission of electron propagated with the physically accurate and computationally expensive Single Scattering model, but with computation time of the default Multiple Scattering method. The model has a parameter that can be adjusted and it effectively scales the scattering cross section. We tuned the parameter to the SNO+ water phase calibration data and implemented the model in the SNO+ analysis framework. By using this model, we resolved a previously observed tension between Monte-Carlo and data in β_{14} parameter for ^{16}N and prompt events of AmBe source (see table 3.3). We also reduced the error in $\cos\theta$ PMT (fig. 3.19) and directionality (fig. 3.18) distributions. These improvements potentially can reduce the systematic errors of the water phase analyses. For example, the total contribution of mentioned factors to the nucleon decay analysis [50] is from 15% to 40%. The implemented method can also be used in the scintillator phase but need to be tuned to a new material. Moreover, these studies may also help to improve the precision of the simulations in new generation Cherenkov light astroparticle detectors, such as Hyper Kamiokande [76], since the detectors will gather more data and extract more precise information, and may be affected by the mismodeling of the angular distribution of Cherenkov light.

In the second part, we developed a code for the simulation of optical crosstalk in SiPMs. We compared simulation results to the measured levels of OCT and light emission from the surface of Hamamatsu VUV4 and FBK HD3 SiPMs and demonstrated the method to make them fit by varying the geometry parameters we do not know precisely. We also listed possible applications of the code such as exploring the influence of the trenches materials on photons propagation, getting the emission spectra of the avalanche photons, prediction of the OCT levels of new models of SiPMs. New measurements are underway at TRIUMF that will be used to further validate the methods and the current code will be also used towards the development of "back-side illuminated" SiPMs [77] targeting keV scale electron detection.

Bibliography

[1] E. P. Cherenkova, "The discovery of the cherenkov radiation," *Nuclear Instruments and Methods in Physics Research Section A: Accelerators, Spectrometers, Detectors and Associated Equipment*, vol. 595, no. 1, pp. 8–11, 2008.

[2] P. Cherenkov, "Vidimoe svechenie chistykh zhidkostei pod deistviem γ-radiatsii," in *Dokl. Akad. Nauk SSSR*, vol. 2, 1934, p. 451.

[3] I. M. Frank and I. E. Tamm, "Coherent visible radiation of fast electrons passing through matter," *Compt. Rend. Acad. Sci. URSS*, vol. 14, no. 3, pp. 109–114, 1937.

[4] P. Cherenkov, "The spatial distribution of visible light produced by rapid electrons," *DAN*, vol. 21, p. 323, 1938.

[5] G. B. Collins and V. G. Reiling, "Cherenkov radiation," *Physical Review*, vol. 54, no. 7, pp. 499 –503, 1938.

[6] H. O. Wyckoff and J. Henderson, "The spatial asymmetry of cerenkov radiation as a function of electron energy," *Physical Review*, vol. 64, no. 1-2, pp. 1 –6, 1943.

[7] H. Kolanoski and N. Wermes, *Particle Detectors: Fundamentals and Applications*. 2020, ch. Cherenkov detectors, pp. 427, 437.

[8] F. Simon, "Silicon photomultipliers in particle and nuclear physics," *Nuclear Instruments and Methods in Physics Research Section A: Accelerators, Spectrometers, Detectors and Associated Equipment*, vol. 926, pp. 85–100, 2019.

[9] K. Ozaki, S. Kazama, M. Yamashita, Y. Itow, and S. Moriyama, "Characterization of new photo-detectors for the future dark matter experiments with liquid xenon," *Journal of Physics: Conference Series*, vol. 1468, no. 1, p. 012 238, 2020.

[10] C. L. Cowan, F. Reines, F. B. Harrison, H. W. Kruse, and A. D. McGuire, "Detection of the free neutrino: A confirmation," *Science*, vol. 124, no. 3212, pp. 103–104, 1956.

[11] G. Danby *et al.*, "Observation of high-energy neutrino reactions and the existence of two kinds of neutrinos," *Phys. Rev. Lett.*, vol. 9, pp. 36–44, 1 1962.

[12] K. Kodama *et al.*, "Observation of tau neutrino interactions," *Phys. Lett. B*, vol. 504, pp. 218–224, 2001. arXiv: hep-ex/0012035.

[13] M. Sajjad Athar *et al.*, "Status and perspectives of neutrino physics," *Prog. Part. Nucl. Phys.*, vol. 124, p. 103 947, 2022.

[14] Y. Fukuda *et al.*, "Evidence for oscillation of atmospheric neutrinos," *Physical Review Letters*, vol. 81, no. 8, pp. 1562–1567, 1998.

[15] Q. R. Ahmad *et al.*, "Measurement of the rate of $\nu_e + d \to p + p + e^-$ interactions produced by ^{8}B solar neutrinos at the Sudbury Neutrino Observatory," *Phys. Rev. Lett.*, vol. 87, p. 071 301, 2001.

[16] Y. Cai, T. Han, T. Li, and R. Ruiz, "Lepton number violation: Seesaw models and their collider tests," *Frontiers in Physics*, vol. 6, 2018.

[17] S. F. King, A. Merle, S. Morisi, Y. Shimizu, and M. Tanimoto, "Neutrino mass and mixing: From theory to experiment," *New Journal of Physics*, vol. 16, no. 4, p. 045 018, 2014.

[18] S. Fukuda *et al.*, "The super-kamiokande detector," *Nuclear Instruments and Methods in Physics Research Section A: Accelerators, Spectrometers, Detectors and Associated Equipment*, vol. 501, no. 2, pp. 418–462, 2003.

[19] M. G. Aartsen *et al.*, "The IceCube Neutrino Observatory: Instrumentation and Online Systems," *JINST*, vol. 12, no. 03, P03012, 2017. arXiv: 1612.05093 `[astro-ph.IM]`.

[20] I. A. Sokalski, "The ANTARES experiment: Past, present and future," in *INFN Eloisatron Project 44th Workshop on QCD at Cosmic Energies: The Highest Energy Cosmic Rays and QCD*, Jan. 2005. arXiv: hep-ex/0501003.

[21] M. Askins *et al.*, "THEIA: an advanced optical neutrino detector," *Eur. Phys. J. C*, vol. 80, no. 5, p. 416, 2020. arXiv: 1911.03501 `[physics.ins-det]`.

[22] S. Agostinelli *et al.*, "Geant4—a simulation toolkit," *Nuclear Instruments and Methods in Physics Research Section A: Accelerators, Spectrometers, Detectors and Associated Equipment*, vol. 506, no. 3, pp. 250–303, 2003.

[23] J. Jackson, *Classical Electrodynamics*, 2nd ed. John Wiley and Sons, 1975.

[24] Geant4 Collaboration. "Book for Application Developers. Cherenkov light." (2022).

[25] L. Urbán, "A model for multiple scattering in GEANT4," CERN, Geneva, Tech. Rep., 2006.

[26] F. Salvat, J. M. Fernandez-Varea, E. Acosta, and J. Sempau, *Penelope - A code system for Monte Carlo simulation of electron and photon transport*. Nuclear Energy Agency of the OECD (NEA): Organisation for Economic Co-Operation and Development - Nuclear Energy Agency, 2001.

[27] V. N. Ivanchenko, O Kadri, M Maire, and L Urban, "Geant4 models for simulation of multiple scattering," *Journal of Physics: Conference Series*, vol. 219, no. 3, p. 032 045, 2010.

[28] M. J. Boschini *et al.*, "Nuclear and non-ionizing energy-loss of electrons with low and relativistic energies in materials and space environment," in *Astroparticle, Particle, Space Physics, Radiation Interaction, Detectors and Medical Physics Applications*, WORLD SCIENTIFIC, 2012, pp. 961–982.

[29] T. Lijian, H. Qing, and L. Zhengming, "Analytic fitting to the mott cross section of electrons," *Radiation Physics and Chemistry*, vol. 45, no. 2, pp. 235–245, 1995.

[30] H. A. Bethe, "Molière's Theory of Multiple Scattering," *Phys. Rev.*, vol. 89, pp. 1256–1266, 6 1953.

[31] J. Fernández-Varea, R. Mayol, J. Baró, and F. Salvat, "On the theory and simulation of multiple elastic scattering of electrons," *Nuclear Instruments and Methods in Physics Research Section B: Beam Interactions with Materials and Atoms*, vol. 73, no. 4, pp. 447–473, 1993.

[32] O. Kadri, V. Ivanchenko, F. Gharbi, and A. Trabelsi, "Geant4 simulation of electron energy deposition in extended media," *Nuclear Instruments and Methods in Physics Research Section B: Beam Interactions with Materials and Atoms*, vol. 258, no. 2, pp. 381–387, 2007.

[33] M. Anderson *et al.*, "Optical calibration of the SNO detector in the water phase with deployed sources," *Journal of Instrumentation*, vol. 16, no. 10, P10021, 2021.

[34] R. J. Komar, "The Effects of Electron Scattering on Cherenkov Light Output," University of British Columbia, Vancouver, Tech. Rep., 1995.

[35] L. Schiff, *Quantum Mechanics*. McGraw-Hill book company, 1949.

[36] K. G. Dedrick, "The Influence of Multiple Scattering on the Angular Width of Čerenkov Radiation," *Phys. Rev.*, vol. 87, pp. 891–896, 5 1952.

[37] M. G. Bowler, "Effects of electron scattering on Cherenkov light output," *Nucl. Instrum. Meth. A*, vol. 378, pp. 463–467, 1996.

[38] V. Albanese *et al.*, "The SNO experiment," *Journal of Instrumentation*, vol. 16, no. 08, P08059, 2021.

[39] J Boger *et al.*, "The sudbury neutrino observatory," *Nuclear Instruments and Methods in Physics Research Section A: Accelerators, Spectrometers, Detectors and Associated Equipment*, vol. 449, no. 1, pp. 172–207, 2000.

[40] V. Flaminio *et al.*, "Current status and future prospects of the SNO+ experiment," *Advances in High Energy Physics*, vol. 2016, p. 6 194 250, 2016.

[41] H. P. K. K., *Technical note*, 2007.

[42] J. Dunmore, "The separation of cc and nc events in the sudbury neutrino observatory," Ph.D. dissertation, 2004.

[43] G. Horton-Smith, "An introduction to glg4sim features," Presented on May 19, 2006, 2006.

[44] M. Dragowsky *et al.*, "The 16n calibration source for the sudbury neutrino observatory," *Nuclear Instruments and Methods in Physics Research Section A: Accelerators, Spectrometers, Detectors and Associated Equipment*, vol. 481, no. 1-3, pp. 284–296, 2002.

[45] Y. Liu, "Ambe source calibration in the SNO+ water phase," 2018.

[46] M. Anderson *et al.*, "Search for invisible modes of nucleon decay in water with the SNO+ detector," *Phys. Rev. D*, vol. 99, p. 032 008, 3 2019.

[47] R. Bayes, "Update on beta14 discrepancy," Laurentian University, Tech. Rep., 2018.

[48] Y. Zhang, "A summary of Beta14 tuning," University of Alberta, Tech. Rep., 2019.

[49] J. Hu, "A measurement of solar neutrinos and the development of reconstruction algorithms for the SNO+ experiment," Ph.D. dissertation, University of Alberta, 2022.

[50] M. Anderson *et al.*, "Search for invisible modes of nucleon decay in water with the SNO+ detector," *Phys. Rev. D*, vol. 99, p. 032 008, 3 2019.

[51] "Photodetectors," in Boston, MA: Springer US, 2002, pp. 545–581.

[52] T. Kaptanoglu, M. Luo, and J. Klein, "Cherenkov and scintillation light separation using wavelength in LAB based liquid scintillator," *Journal of Instrumentation*, vol. 14, no. 05, 2019.

[53] J. Dunger, E. J. Leming, and S. D. Biller, "Slow-fluor scintillator for low energy solar neutrinos and neutrinoless double beta decay," *Physical Review D*, vol. 105, no. 9, 2022, ISSN: 2470-0029.

[54] T. Abe, "R&D status of HAPD," *PoS*, vol. PD09, p. 014, 2010. DOI: 10.22323/1.090.0014.

[55] J. B. McLaughlin *et al.*, *Characterisation of SiPM Photon Emission in the Dark*, 2021.

[56] *KETEK GMBH: SiPM Technology*, http://www.ketek.net/products/sipm-technology/, Accessed: 2022-06-24.

[57] H. P. K. K., *Technical note. mppc.* 2021.

[58] P. BUZHAN *et al.*, "The advanced study of silicon photomultiplier," in pp. 717–728.

[59] H. P. K. K., *Silicon Photomultiplier: Operation, Performance Possible Applications.* Accessed: 2022-06-24, 2021.

[60] I. Rech *et al.*, "Optical crosstalk in single photon avalanche diode arrays: A new complete model," *Opt. Express*, vol. 16, no. 12, pp. 8381–8394, 2008.

[61] M. L. Knoetig, J. Hose, and R. Mirzoyan, "Sipm avalanche size and crosstalk measurements with light emission microscopy," *IEEE Transactions on Nuclear Science*, vol. 61, no. 3, pp. 1488–1492, 2014.

[62] L Gallego, J Rosado, F Blanco, and F Arqueros, "Modeling crosstalk in silicon photomultipliers," *Journal of Instrumentation*, vol. 8, no. 05, P05010–P05010, 2013.

[63] J. Rosado and S. Hidalgo, “Characterization and modeling of crosstalk and afterpulsing in hamamatsu silicon photomultipliers,” *Journal of Instrumentation*, vol. 10, no. 10, P10031–P10031, 2015.

[64] A. N. Otte, “Observation of vhe γ–rays from the vicinity of magnetized neutron stars and development of new photon-detectors for future ground based γ-ray detectors,” Ph.D. dissertation, 2007.

[65] M. P. Bora, “Photon cross-talk of optical photons in silicon photo-multipliers,” 2021.

[66] D. Minchenko, JADDE Collaboration. “Optical crosstalk in a SiPM G4-based simulation.” (2022), [Online]. Available: https://geant4-userdoc.web.cern.ch/UsersGuides/ForApplicationDeveloper.

[67] D. Minchenko, JADDE Collaboration. “Optical crosstalk in a SiPM G4-based simulation analysis.” (2022), [Online]. Available: https://github.com/dmytro-cloud/CrossTalkSim.

[68] Geant4 Collaboration. “Book for Application Developers. Boundary process.” (2022).

[69] P. G. Snyder, Y.-M. Xiong, J. A. Woollam, E. R. Krosche, and Y. Strausser, “Characterization of polycrystalline silicon thin-film multilayers by variable angle spectroscopic ellipsometry,” *Surface and Interface Analysis*, vol. 18, no. 2, pp. 113–118, 1992.

[70] F. Roozeboom, *Advances in rapid thermal and integrated processing*. Springer Science & Business Media, 2013, vol. 318.

[71] W. S. M. Warner. “RI Tungsten.” (2009).

[72] F. Vachon, “Conception de photodiodes à avalanche monophotonique sensibles aux photons ultraviolets pour les détecteurs de la physique des particules dans les gaz nobles liquéfiés,” Ph.D. dissertation, 2021.

[73] G. Gallina *et al.*, “Characterization of sipm avalanche triggering probabilities,” *IEEE Transactions on Electron Devices*, vol. 66, no. 10, pp. 4228–4234, 2019.

[74] G. Gallina *et al.*, “Characterization of the hamamatsu vuv4 mppcs for nexo,” *Nuclear Instruments and Methods in Physics Research Section A: Accelerators, Spectrometers, Detectors and Associated Equipment*, vol. 940, pp. 371–379, 2019.

[75] J. Martin, “Characterization of laser-driven photon emission in silicon photomultipliers at triumf,” Presented at CAP Congress 2022 Hamilton, ON, Canada, 2022.

[76] K. Abe *et al.*, *Letter of Intent: The Hyper-Kamiokande Experiment — Detector Design and Physics Potential —*, 2011.

[77] W.-S. Choong and S. E. Holland, “Back-side readout silicon photomultiplier,” *IEEE Transactions on Electron Devices*, vol. 59, no. 8, pp. 2187–2191, 2012. DOI: 10.1109/TED.2012.2200684.

Appendix A: SiPM geometry variation

In Chapter 4 we discuss a possible influence of varying geometry and material parameters in the simulation on the optical crosstalk. In this appendix we put examples of effect of varying Hamamatsu VUV4 SiPM (HPK) geometry. We vary trenches depth and width on fig. A.1 and also trying another avalanche region depth and width on fig. A.2.

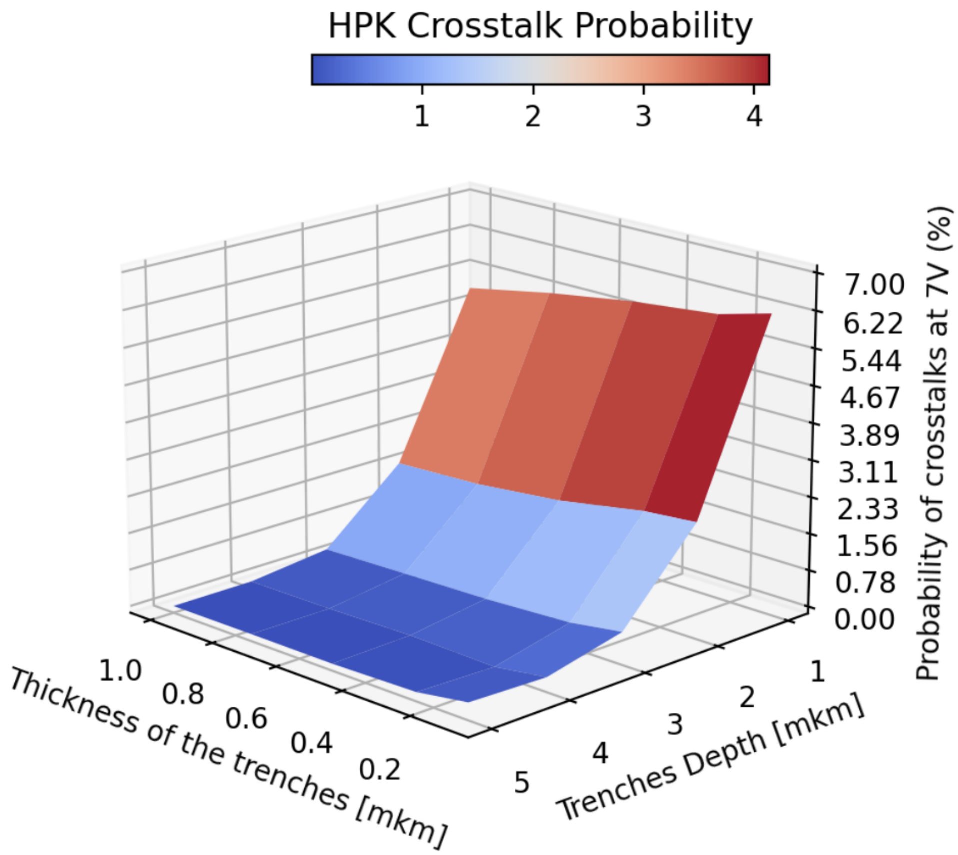

Figure A.1: Optical cross talk as the function of trenches depth and width.

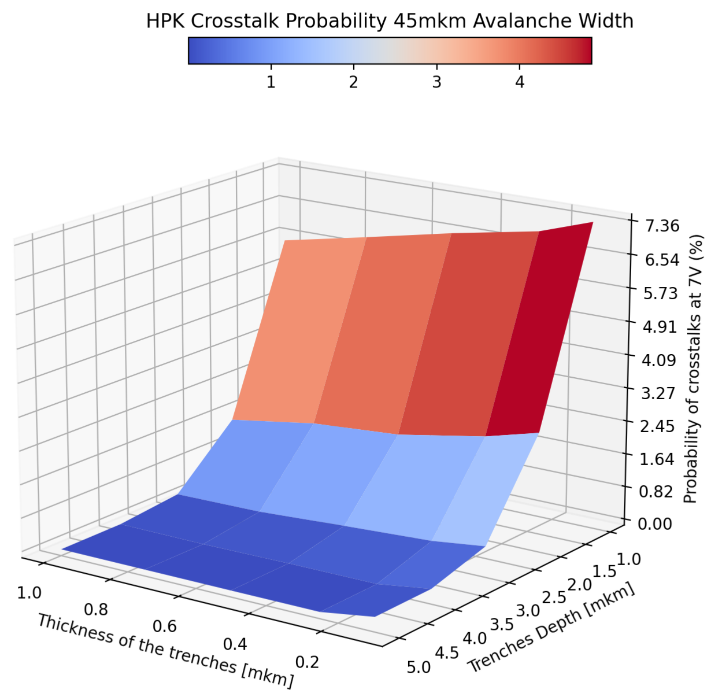

Figure A.2: Optical cross talk as the function of trenches depth and width with a different avalanche region depth.

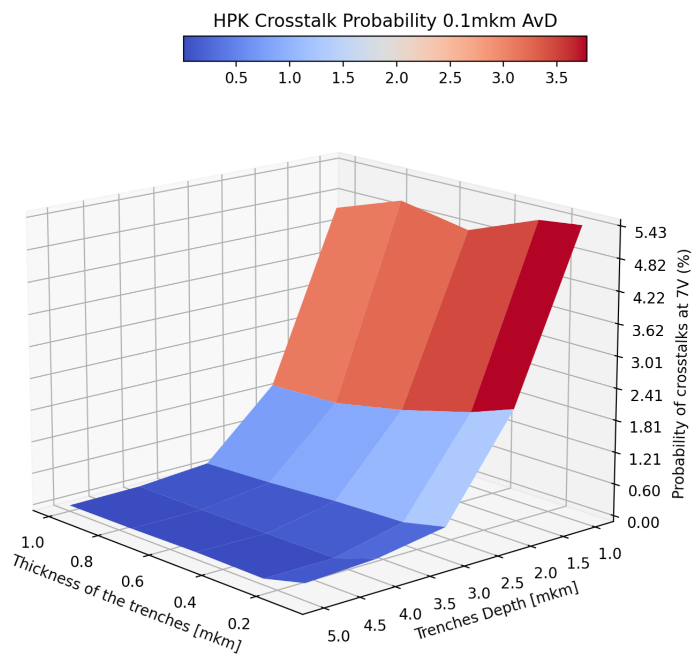

Figure A.3: Optical cross talk as the function of trenches depth and width with a different avalanche region width

Appendix B: Selection criteria

The modifications of the code and analysis were done and calibrated with RAT 6.18.12. Using other versions of RAT may need recalibration and different value of α parameter. Conditions that will replicate the same selection for ^{16}N and AmBe sources as in chapter 3.

B.1 ^{16}N selection

For ^{16}N we used central run 107055 and selection for the events:

- FitValid and WaterValid
- ((dcApplied & 0xFB0000017FFE) & dcFlagged) == (dcApplied & 0xFB0000017FFE)
- (triggerWord & 0x6)
- $-0.5 < \beta_{14} < 1.5$
- Event tagged by calibration source
- nhits > 5

B.2 AmBe selection

For AmBe we used central run 109133 with the selection criteria:

- FitValid and WaterValid
- ((dcApplied & 0xFB0000017FFE) & dcFlagged) == (dcApplied & 0xFB0000017FFE))

- (triggerWord & 0x401400) == 0x0 && (triggerWord != 0x40)
- $-0.5 < \beta_{14} < 1.5$

For prompt specifically:

- NhitCleaned ≥ 12

For delayed coincidence:

- Nhits ≥ 4
- timeDiff $< 200\mu$s
- posDiff < 1m